NASA TM X-1306

EXPERIMENTAL INVESTIGATION OF LAMINAR HEAT-TRANSFER CHARACTERISTICS OF A MANNED LIFTING ENTRY VEHICLE AT A MACH NUMBER OF 20

By William D. Harvey

Langley Research Center
Langley Station, Hampton, Va.

NATIONAL AERONAUTICS AND SPACE ADMINISTRATION

L-4845

EXPERIMENTAL INVESTIGATION OF LAMINAR HEAT-TRANSFER CHARACTERISTICS OF A MANNED LIFTING ENTRY VEHICLE AT A MACH NUMBER OF 20*

By William D. Harvey
Langley Research Center

SUMMARY

An experimental investigation has been conducted to determine the laminar heat-transfer characteristics of a basic version of a manned lifting entry vehicle (designated HL-10) having a hypersonic maximum lift-drag ratio of about 1. Tests were conducted in the Langley hotshot tunnel with nitrogen as the test medium at a nominal Mach number of 20 and a Reynolds number (based on model length) of 0.20×10^6 for angles of attack from 10° to 50° and elevon deflection angles of 0°, 15°, and 30°.

Experimental heat-transfer coefficients are compared with theoretical heat-transfer coefficients derived from infinite swept cylinder concepts. The heat transfer along the curved-lower-surface midline was in good agreement with that obtained by theory for an angle of attack of 50° and for all elevon deflection angles but was not in as good agreement for an angle of attack of 30°. Isolated cylinder theory predicted body-leading-edge heating values which were in fair agreement with the measured values for a forward chordwise station (one-eighth of model length behind nose), but these predicted values were always greater than the measured values at the remaining stations. The largest discrepancy occurred at one-half the model length. The assumed separation and reattachment on the lower surface of the 30° deflected elevon produced high values in heating on the lower surface of the elevon that were approximately an order of magnitude larger than the values obtained for the undeflected elevon for an angle of attack of 50°.

In general, good agreement was obtained between the present results and the laminar heating results from previous investigations at a Mach number of 8 and at nearly the same Reynolds number. Some disagreement did occur, however, in the cylindrical leading-edge region and for the lower surface of the 30° deflected elevon.

INTRODUCTION

The Langley Research Center is conducting a general research program using a manned lifting entry vehicle (designated HL-10) that has a hypersonic maximum lift-drag

*Title, Unclassified.

ratio of about 1. A general discussion of the vehicle geometry and performance along with some of the results of several Langley studies (including force and heat-transfer tests) may be found in reference 1. Experimental pressure distributions on the HL-10 configuration at a Mach number of 19.5 may be found in reference 2.

Laminar heating characteristics for a basic version of the HL-10 configuration at a Mach number of 8 are presented in reference 3 for Reynolds numbers (based on model root chord) from 0.24×10^6 to 2.70×10^6, angles of attack from 20° to 60°, and elevon deflection angles of 0°, 30°, and -60°. Turbulent heating characteristics of the configuration at a Mach number of 8 are presented in reference 4 for a Reynolds number (based on model root chord) from 2.70×10^6 to 6.58×10^6, angles of attack from 0° to 60°, and elevon deflection angles of 0°, 15°, and 30°. Some laminar heating characteristics were also obtained in reference 4 for a Reynolds number of 6.58×10^6 and for angles of attack from 0° to 40°. Since the windward surface of the vehicle is expected to experience high heating rates during reentry, it was desirable to extend the Mach number range of the heating characteristics for design purposes and to determine the effect of increasing the Mach number. Therefore, the present investigation was undertaken to obtain laminar aerodynamic heating characteristics for a nominal Mach number of 20 and a Reynolds number (based on model length) of 0.20×10^6. The investigation was made on an 8-inch (20.32 cm) model in the Langley hotshot tunnel at angles of attack from 10° to 50° and with elevon deflection angles of 0°, 15°, and 30°. A comparison of the experimental data along the lower-surface midline with those predicted from laminar stagnation-point heating theory is presented. Also presented are the spanwise distributions for five chordwise stations. For the first four of these stations, these distributions are compared with results from isolated cylinder theory. A further comparison of the present data with those of references 3 and 4 is made.

SYMBOLS

The units used for physical quantities in this paper are given both in the U.S. Customary Units and in the International System of Units (SI). Factors relating the two systems are given in reference 5. For convenience, conversion factors for the physical quantities used in the present investigation are presented in the appendix.

A stagnation-point velocity gradient

a speed of sound based on stagnation temperature

C_p pressure coefficient, $\dfrac{p - p_\infty}{\rho_\infty V_\infty^2/2}$

$C_{p_{t,2}}$	pressure coefficient at stagnation point
c	maximum model length (excluding tip fins) or maximum model chord (see fig. 1)
c_e	elevon chord
c_s	specific heat of heat-sensing material
D_n	model nose diameter
h	heat-transfer coefficient
$\bar{h}$	heat-transfer coefficient without pressure gradient ($dp/dx = 0$)
h_o	calculated laminar stagnation-point heat-transfer coefficient for sphere having same radius as model nose
K_3	pressure-gradient correction factor (see eq. (9))
k_w	thermal conductivity at wall
M_l	local Mach number
M_∞	free-stream Mach number
N_{Nu}	Nusselt number, $\frac{hx'}{k_w}$
p	pressure
$p_{t,1}$	reservoir pressure following arc discharge
$p_{t,2}$	stagnation pressure behind normal shock
p_w	wall pressure
p_∞	free-stream pressure
$\dot{q}$	heat-transfer rate
r	radius

R_c free-stream Reynolds number, $\frac{\rho_\infty V_\infty c}{\mu_\infty}$

R_l local Reynolds number based on velocity at edge of boundary layer and kinematic viscosity at wall, $\frac{V_l x'}{\nu_w}$

s spanwise distance measured along body surface normal to lower-surface midline

T_{aw} adiabatic-wall temperature

T_l local temperature

$T_{t,1}$ reservoir temperature following arc discharge

$T_{t,2}$ stagnation temperature behind normal shock

$T_{t,2,n}$ stagnation temperature based on component of flow normal to leading edge or windward surface

T_w wall temperature

t time

V_l local velocity at edge of boundary layer

V_∞ free-stream velocity

x,y,z model coordinates (see fig. 1)

x' longitudinal coordinate from stagnation point measured from nose along body surface

x_e distance along elevon

α angle of attack

γ ratio of specific heats

δ_e elevon deflection angle in plane normal to hinge line, positive when trailing edge is down

η	temperature recovery factor
$\mu_{t,2}$	stagnation viscosity behind normal shock
$\mu_{t,2,n}$	stagnation viscosity based on component of flow normal to leading edge or windward surface
μ_w	viscosity at wall
μ_∞	free-stream viscosity
ν_w	kinematic viscosity at wall
ρ_s	density of model skin material
ρ_w	density at wall
ρ_∞	free-stream density
τ_s	thickness of model skin material

APPARATUS AND TESTS

Model

The model used in the present investigation was that for a basic version of a manned lifting entry vehicle (designated HL-10) having a hypersonic maximum lift-drag ratio of about 1. The model was 8 inches (20.32 cm) long; other pertinent dimensions are given in figure 1. The thermocouple locations on the model are presented in figure 2 and table I. Body ordinates are given in table II. A complete description of model geometry is presented in reference 3.

Model construction.- The model was constructed in two parts consisting of an upper and lower half. (See ref. 6 for a more detailed discussion of model construction.) Each half was constructed by pressing sheets of 1/64-inch-thick (0.397 mm) stainless steel into a female mold with a male mandrel. Holes (0.25 inch (6.35 mm) in diameter) were then drilled in the structure wherever heat-transfer measurements were desired. The two halves were then covered with a thin stainless-steel skin (0.004 inch (101.6 μm) for the lower surface and 0.002 inch (50.8 μm) for the upper surface) which formed calorimeters at the hole locations once thermocouple wires were attached. The upper and

lower halves were attached with screws to an additional internal structure. The hatch cover and the elevons were also attached with screws. (See fig. 3.)

The same canted tip fins employed in reference 3 were used in the present investigation. The center dorsal fin previously used was replaced by a wedge-shaped sting mounted at 75° to the model center line, as shown in figure 1.

Three separate elevons were constructed to provide elevon deflection angles of 0°, 15°, and 30°. Upper and lower surfaces of the elevons were made in one piece and were sealed on both sides and along the trailing edge after the instrumentation was installed.

Model instrumentation.- Chromel-alumel thermocouple wires 0.001 inch (0.025 mm) in diameter were welded to the back surface of the thin stainless-steel-skin sensing surface through the drilled holes of the support structure. A calorimeter was thus formed at each location. The locations of the instrumented stations, shown in figure 2, are similar to those of references 3 and 4. Seventeen of the seventy thermocouples were located along the upper and lower curved surfaces at the midline of the model. The majority of the remaining thermocouples are located in the spanwise direction mainly at seven chordwise locations (x/c of 0.125, 0.250, 0.500, 0.750, 0.875, 0.950, and 1.000). For each deflection, the elevon was instrumented both on the upper and lower surfaces. Skin thickness at each thermocouple location was measured and subsequently used in the data reduction. All thermocouple leads were contained within the model and sting.

Tests and Data Reduction

The model was tested in nitrogen in the Langley hotshot tunnel. A detailed description and calibration of this tunnel are given in reference 7. The nominal reservoir pressure, temperature, and enthalpy for the present tests were 10000 lbf/in^2 (68.947 MN/m^2), 4940° F (3000° K), and 1600 Btu/lbm (3.72 km^2/sec^2). The nominal free-stream Mach number was 20 and the Reynolds number (based on model length) was approximately 0.20×10^6. These test conditions were calculated by use of the real-nitrogen data-reduction method of reference 8. The assumption of vibrational equilibrium of the gas was made for the present test conditions. (See discussion in ref. 7.)

The energy balance equation for a thin calorimeter with conductive and radiative heat losses assumed to be negligible was used to reduce the thermocouple measurements to heat-transfer rates:

$$\dot{q} = \rho_s c_s \tau_s \frac{dT_w}{dt} \tag{1}$$

Since the thickness τ_s, specific heat c_s, and density ρ_s of the heat-sensing material were known, only the time derivative of the average surface temperature dT_w/dt was necessary to obtain the heat-transfer rates. This derivative was actually determined by

measuring the slope of each thermocouple-output oscillograph trace at discrete time intervals in terms of galvanometer deflection. The paper speed of each oscillograph record, the sensitivity of each chromel-alumel thermocouple, and the calibration for each thermocouple-galvanometer circuit were used in equation (1) to determine dT_w/dt.

Heat-transfer coefficients were calculated from the equation

$$h = \frac{\dot{q}}{T_{aw} - T_w} \tag{2}$$

where the adiabatic-wall temperature T_{aw} was calculated from

$$T_{aw} = T_l\left(1 + \eta \frac{\gamma - 1}{2} M_l^2\right)$$

and a value of 0.85 was used for the recovery factor η. The local temperature and Mach number were determined by use of the experimental pressures from reference 2 and with the assumption that the flow expanded isentropically from the pressure behind a normal shock to the static pressure at the point in question. Free-stream static pressure was assumed to exist in the leeward region on the model.

The short tunnel test times (approximately 0.1 second) of the present investigation tended to minimize all heat losses from the calorimeter thermocouples. In order to reduce heat losses further, the data were computed at elapsed test times of less than 30 milliseconds; and, therefore, no corrections for heat-conduction losses were made to the results. Since the temperature rise of the sensing material at these short periods of elapsed test times was small (at the nose, on the order of 30° K above room temperature), constant values of ρ_s and c_s were used.

The heat-transfer results are presented as the ratio h/h_o, where h_o is the theoretical stagnation-point heat-transfer coefficient for a sphere having the same radius as the nose of the HL-10 model. The purpose of using this particular heat-transfer coefficient was to enable a direct comparison between the present data and the data of references 3 and 4 as well as to correlate the present laminar data. The values of h_o were calculated from the following equation adapted from reference 9:

$$h_o = \sqrt{\frac{\rho_w}{\mu_w}} \sqrt{A}\left(\frac{N_{Nu}}{\sqrt{R_l}}\right) k_w \tag{3}$$

For free-stream Mach numbers greater than 2, a general expression for the stagnation-point velocity gradient A applicable to both two-dimensional flow and axially symmetric flow can be derived from the pressure coefficient written in a modified Newtonian flow form:

$$\frac{C_p}{C_{p_{t,2}}} = \cos^2\left(\frac{x'}{r}\right) \tag{4}$$

By use of Bernoulli's relation and equation (4), the following expression for the velocity gradient is obtained:

$$A = \frac{a}{r}\sqrt{\frac{2}{\gamma}\left(1 - \frac{p_\infty}{p_{t,2}}\right)} \tag{5}$$

where $p_\infty/p_{t,2}$ is the Rayleigh pitot formula given by the relation

$$\frac{p_\infty}{p_{t,2}} = \left[\frac{2}{(\gamma + 1)M_\infty^2}\right]^{\frac{\gamma}{\gamma-1}}\left[\frac{2\gamma M_\infty^2 - (\gamma - 1)}{\gamma + 1}\right]^{\frac{1}{\gamma-1}} \tag{6}$$

As the Mach number becomes large, equation (5) reduces to

$$A = \frac{a}{r}\sqrt{\frac{2}{\gamma}} = \frac{V_\infty}{r}\sqrt{\frac{\gamma - 1}{\gamma}} \tag{7}$$

which is an approximation for the velocity gradient for large Mach numbers.

Values of h_o were calculated for each tunnel test. A variation of approximately 1 percent occurred in the values because of the slight run-to-run variations of stagnation conditions. For the nominal initial test conditions of $p_{t,1} = 10000$ lbf/in^2 (68.947 MN/m^2) and $T_{t,1} = 3000^\circ$ K, the value calculated for h_o was 0.038 Btu/ft^2-sec^2-$^\circ$K (431.3 W/m^2-$^\circ$K).

THEORY

The theory applied in the present investigation was the same as that used in reference 3 for the heating distribution on the lower-surface midline and on the leading edge of the body. In using the infinite swept cylinder concepts, the model was considered to be divided into spanwise sections and the heat transfer was calculated for a cylinder having the same cross section as the body and on the tangent to the body. Only the normal component of the flow was considered in accordance with the sweepback principle, and streamline divergence was not taken into account. Heat transfer to the 90° segment of a cylinder forming the leading edge was calculated as though it were part of an isolated infinite swept cylinder.

Heating Distribution Along Midline

An expression adapted by Bertram and Everhart from the Fay and Riddell relation for laminar stagnation-point heating was used to calculate the heating distribution along

the midline of the curved lower surface of the model. In the notation of the present paper, this equation (eq. (10) of ref. 10) may be written as follows:

$$\frac{h}{h_o} \approx \frac{\sin \alpha}{\sqrt{2}} \sqrt{\left(\frac{\mu_{t,2,n}}{\mu_{t,2}}\right)^{0.8} \left(\frac{T_{t,2}}{T_{t,2,n}}\right)^{0.3} \frac{A}{s/(D_n - 0.285)}} \tag{8}$$

where

$$\frac{T_{t,2}}{T_{t,2,n}} = \frac{1 + \frac{\gamma - 1}{2} M_\infty{}^2}{1 + \frac{\gamma - 1}{2}(M_\infty \sin \alpha)^2}$$

The velocity gradient required in this equation was obtained from reference 10. The cylinder cross sections used in the calculations were assumed to have circular shapes rather than slightly elliptical shapes, but the differences were assumed negligible.

Heating Distribution on Body Leading Edge

Stagnation-line heating on the body leading edge was calculated by also using equation (10) of reference 10 (presented as eq. (8) herein). The theory of Lees (ref. 11) was used to obtain the heating distribution around the 90^o segment.

Heating Distribution on Elevon

The hypersonic similarity theory was used to calculate the elevon heating distribution for comparison with the experimental results. Reference 12 shows that for hypersonic flow, where the Prandtl number is equal to unity and where n (exponent of $p_w \propto x^n$) may have positive or negative values, the heat-transfer coefficients may be written as the ratio

$$\frac{h}{\bar{h}} = K_3 \sqrt{\frac{p_w}{p_\infty}} \tag{9}$$

where $\bar{h}$ represents the value for the heat-transfer coefficient in which the pressure gradient is zero. The coefficient K_3 is a pressure-gradient correction factor presented in reference 12 as a function of n. Pressure distributions required in equation (9) were obtained from the experimental results of reference 2.

The theoretical calculations were made for the heating distribution at the elevon midchord with the assumption that the flow on the elevons had been treated by a normal shock at the nose, by an expansion over the body, and by an oblique shock at the elevon. Schlieren photographs, in references 2 and 13, were used to obtain the deflected elevon shock angles to assist in calculating the local flow conditions.

RESULTS AND DISCUSSION

In the present investigation, the solid lines used for fairing the data are to be considered as estimates of the trends of the heat-transfer coefficients since insufficient data points were available to establish absolute magnitudes. Since elevon deflection had no effect on the data over the first 75 percent of the model, only the data demonstrating a variation in heating due to elevon deflection are presented for more than one elevon deflection.

Distribution of Heating Along the Midline

The ratio of the measured heat-transfer coefficient along the midline of the model to the calculated stagnation-point heat-transfer coefficient for a sphere having a radius the same as that of the nose of the model is presented for angles of attack from 10° to 50° in figures 4, 5, and 6 for elevon deflection angles of 0°, 15°, and 30°, respectively. Negative values of x/c represent stations along the upper-surface midline of the model and positive values represent stations along the curved-lower-surface midline. Also, shown in figures 4, 5, and 6 are the heat-transfer distributions determined from the most inboard row of thermocouples (thermocouples 59, 60, and 61 on the upper surface of the elevon and thermocouples 62, 63, and 64 on the lower surface). The elevon data are presented to show the difference between the heating level on the elevons and the heating level on the lower surface of the body. From the level and distribution of the data obtained in the present investigation, the heating appears to be laminar (similar to that of ref. 3).

The theoretical results for the distribution of heating along the midline are in good agreement with the average experimental data for all elevon deflection angles for $\alpha = 50^{\circ}$ but are not in as good agreement for $\alpha = 30^{\circ}$. (See figs. 4 to 6.) Agreement between the experimental results and theory is possibly fortuitous, as was also pointed out in reference 3. Much of the problem of predicting the heat transfer to a delta planform configuration is the changing flow pattern with increasing angle of attack; simple approaches to predicting the heat transfer on a flat delta wing have been shown in reference 10 to be successful if the flow pattern peculiar to the angle-of-attack range under consideration is taken into account.

Figure 7 is a summary plot of heat-transfer distribution along the midline for three representative angles of attack and for elevon deflection angles of 0°, 15°, and 30°. It may be seen from figure 7 that the repeatability is within about ±5 percent. No outstanding differences due to the elevon deflection are indicated by the data. The fairing represents the average heating distribution for all data points.

A comparison of the present Mach 20 lower-surface midline data for angles of attack from 10° to 50° and for $\delta_e = 0^{\circ}$ with the Mach 8 laminar-heat-transfer data of

references 3 and 4 is presented in figure 8. It should be noted that local conditions used for the reduction of data in references 3 and 4 were calculated from Newtonian theory pressure distributions. However, since good agreement was generally shown to exist between the experimental pressure distributions and the Newtonian theory pressure distributions in reference 2, it would make little difference whether the measured or Newtonian pressures were used to calculate local conditions and local adiabatic-wall temperatures. Therefore, because the measured pressures were available (ref. 2), they were used in the present data reduction. In general, the present results agree with those of references 3 and 4 with the exception of the results for $\alpha = 30^{\circ}$ and $\alpha = 40^{\circ}$. For those angles of attack, the heat-transfer distributions of reference 3 are approximately one-third greater than those of the present investigation. There is also some disagreement between the data of reference 3 and those of reference 4 for an angle of attack of 30°. Furthermore, on the lower surface near the nose ($x/c < 0.075$), the present results are somewhat different from those of references 3 and 4 for all angles of attack. The exact cause of this difference is not known; however, inaccuracies in thermocouple location would account for significant differences in h/h_0 in this region where gradients in heating coefficients are large.

Spanwise Distribution of Heating

The experimental spanwise heating distributions at five chordwise stations (x/c of 0.125, 0.250, 0.500, 0.750, and approximately 0.950) are presented in figure 9 for $\delta_e = 0^{\circ}$. In figures 10 and 11, the spanwise distributions are presented for $\delta_e = 15^{\circ}$ and $\delta_e = 30^{\circ}$, respectively. Since no outstanding differences in heating due to elevon deflection had been observed for the first four chordwise stations (see fig. 12 for two representative stations), only the results at $x/c \approx 0.950$ are presented in figures 10 and 11.

The magnitude of heating in the spanwise direction (see figs. 9(a) to 9(b)) is seen to increase to a peak value on the leading edge and then decrease for increasing values of s/D_n. Also, the heating levels decrease for increasing chordwise stations. Spanwise heating on the lower surface of an undeflected elevon and on a tip fin is shown in figure 9(e). The effect of elevon deflection on the heating may be seen by comparing figure 9(e) for $\delta_e = 0^{\circ}$ with figures 10 and 11 for $\delta_e = 15^{\circ}$ and $\delta_e = 30^{\circ}$. The maximum experimental heat-transfer coefficient on the lower surface of the elevon when deflected 30° is about 1.24 times the theoretical sphere stagnation-point heat-transfer coefficient for $\alpha = 50^{\circ}$ (see fig. 11); whereas the maximum experimental value on the lower surface of the undeflected elevon is 0.15 times the theoretical value for the same angle of attack and station (see fig. 9(e)). Heating on the tip fin is relatively unaffected by elevon deflection and is discussed in more detail subsequently.

The theoretical results obtained from isolated cylinder theory are compared with the experimental results in figures 9(a) to 9(d) for $\alpha = 30^{\circ}$ and $\alpha = 50^{\circ}$. The theoretical peak heat-transfer coefficients on the cylindrical leading-edge section are higher than the experimental results for all chordwise stations except $x/c = 0.125$. For this station (see fig. 9(a)), the theoretical curve for $\alpha = 50^{\circ}$ falls below the data, and that for $\alpha = 30^{\circ}$ is in good agreement with the data. At $x/c = 0.500$ (fig. 9(c)), the theoretical peak heat-transfer coefficient for $\alpha = 50^{\circ}$ and for $s/D_n = 1.6$ is about one-half greater than the faired data. In reference 3, the isolated cylinder theory results were always higher than experimental results. The agreement between theory and experimental data in the present investigation for $x/c = 0.125$ is fortuitous since the theory is not expected to give good agreement in the nose region and, in fact, should give better agreement farther downstream on the cylindrical leading-edge section; nevertheless, poorer agreement was indicated between the experimental and theoretical results for the other stations, with the largest discrepancy occurring at the midchord station.

A comparison of the present experimental spanwise heat-transfer distribution with the laminar-heat-transfer results obtained at a Mach number of 8 in the investigations of references 3 and 4 for chordwise stations $x/c = 0.125$ and $x/c = 0.500$ is presented in figure 13 for $\delta_e = 0^{\circ}$. In general, for $x/c = 0.125$ (fig. 13(a)), the experimental results of references 3 and 4 fall below the present results in the cylindrical leading-edge region, with the largest disagreement occurring at $\alpha = 50^{\circ}$. At this high angle of attack, the estimated peak heating in the leading-edge region at $s/D_n = 0.4$ from the data of reference 3 is about seven-eighths of the peak heating as indicated by the solid lines through the present data points. Fair agreement exists for values of s/D_n greater than 0.8. For $x/c = 0.500$ (fig. 13(b)), the data of references 3 and 4 are generally higher than the present data along the lower surface, around the cylindrical leading edge, and along the upper surface of the body.

Heating Distribution on Elevons

Chordwise heat-transfer distributions on the lower surface of the elevons for deflection angles of 0°, 15°, and 30° are presented in figure 14 for angles of attack from 10° to 50°. The variation of the heat-transfer coefficient with the chordwise station on the elevon $(x_e/c_e \approx 0.25, 0.50, \text{and } 0.75)$ is shown for three spanwise locations $(s/D_n = 1.14, 1.57, \text{and } 2.02)$. The spanwise heat-transfer distributions on the elevons for the same values of α and x_e/c_e are presented in figures 9(e), 10, and 11, for elevon deflection angles of 0°, 15°, and 30°, respectively. It is suspected that an elevon deflection of 30° causes laminar separation on the lower surface ahead of the elevons and reattachment on the elevons. Pressure distributions presented in reference 2 tend to support the existence of this flow separation and reattachment. Heat-transfer coefficients on the 30° deflected elevon lower surface (fig. 14) are as much as an order of magnitude greater than those

on the undeflected elevon and this increased heating is caused by what is assumed to be flow reattachment. Results obtained with temperature-sensitive paint (ref. 3) indicated that a region of high heating was observed to cross the elevons diagonally, near midchord of the elevon; this diagonal region was believed to be the reattachment area.

A summary of the heat-transfer distributions as determined from measurements at all instrumented stations on the lower surface of the elevons is presented in figure 15 for each test angle of attack and for the three elevon deflections. The heat-transfer coefficients are seen to increase both with increasing angle of attack and elevon deflection. The experimental results are compared with the hypersonic similarity theory (ref. 12). In general, the theory agrees with the experimental data trend over most of the angle-of-attack range for both the 0° and 15° deflected elevons. (See figs. 15(a) and 15(b).) For $\delta_e = 30^{\circ}$ (fig. 15(c)), however, the theory underpredicts the average experimental results by as much as four-fifths at $\alpha = 50^{\circ}$, but the prediction improves with decreasing angle of attack and is satisfactory at $\alpha = 20^{\circ}$. The theory shown is presented in figure 15(c) for comparison purposes only since it is believed that the flow is separated ahead of and reattached on the 30° deflected elevon, and, therefore, the theory is not strictly applicable.

A summary of the heat-transfer distributions as determined from measurements at all instrumented stations on the upper surface of the 0° and 30° deflected elevons is presented in figure 16 for the test angle-of-attack range. (No measurements were made on the upper surface of the 15° deflected elevon.) The heat transfer to the upper surface of the elevons for $\delta_e = 0^{\circ}$ (fig. 16(a)) and $\delta_e = 30^{\circ}$ (fig. 16(b)) generally decreases with increasing angle of attack.

Results obtained in the present investigation on the lower surface of the elevons are compared with those obtained in the investigation of reference 3 in figure 17 for angles of attack of 20°, 30°, and 40° and for elevon deflection angles of 0° and 30°. In general, the present results show good agreement with the reference data for the undeflected elevons; however, when the elevons were deflected 30°, the agreement was poor. The discussion on agreement between the present results and those of reference 3 is largely based on the magnitude of the heating distributions on the elevons as indicated by the solid lines connecting the data points. It is very possible that separation and reattachment could occur at entirely different locations for the different test conditions. For instance, wall-temperature—stagnation-temperature ratio in conjunction with local Mach number could have a large effect on the location of separation and reattachment.

Heating Distribution on Tip Fin

The heat-transfer distribution on the leading edge of the tip fin is shown in figure 18, which presents the undeflected-elevon results as being representative of the tip-fin heating distributions for an angle-of-attack range from 10° to 50°. The highest

experimental heat-transfer coefficient on the tip-fin leading edge occurred at $\alpha = 10^{\circ}$ and varied from about 0.36 times the theoretical sphere stagnation-point heat-transfer coefficient at the forward thermocouple location to about 0.27 times the theoretical heating at the most rearward thermocouple location. Increases in angle of attack resulted in corresponding decreases in heating because of increases in the effective sweep angle.

The previously discussed results agree with the results of reference 3. The normal operational angle-of-attack range for the HL-10 is anticipated to be from about 25° to 50°, a range which would include the angle of attack at maximum lift-drag ratio. For this test angle-of-attack range, the heating on the leading edges of the tip fins is seen to be relatively low.

CONCLUSIONS

An investigation to determine the laminar heat-transfer characteristics of a basic version of a manned lifting entry vehicle (designated HL-10) has been performed in the Langley hotshot tunnel with nitrogen as the test medium at a nominal Mach number of 20 and a Reynolds number (based on body length) of 0.20×10^6. Results were obtained for angles of attack from 10° to 50° and elevon deflection angles of 0°, 15°, and 30°. Analysis of these results and comparisons with theoretical heating results and with results from previous experimental investigations at a Mach number of 8 have led to the following conclusions:

1. For all elevon deflection angles, the average heat transfer measured along the curved-lower-surface midline of the body was in agreement with that calculated for a tangent infinite swept cylinder assumed to have the same cross section as the body for an angle of attack of 50° but was in disagreement for an angle of attack of 30°.

2. The theoretical spanwise heating predicted by considering the leading-edge segment to be an isolated swept cylinder was fortuitously in good agreement with the experimental heating near the nose but was in poor agreement for the remaining stations farther downstream for all elevon deflection angles. The largest discrepancy occurred at the midchord station.

3. Downward elevon deflection of 30° apparently caused laminar separation and reattachment on the lower surface of the elevons. The heat-transfer coefficients were found to be an order of magnitude greater than those for the undeflected elevons, probably because of the flow reattachment.

4. In general, good agreement was obtained between the present heating distributions along the lower-surface midline, in the spanwise direction, and on the elevons and the results from previous investigations at a Mach number of 8 and at nearly the same Reynolds number. Some disagreement did occur, however, in the cylindrical leading-edge region and for the lower surface of the 30° deflected elevon.

Langley Research Center,
National Aeronautics and Space Administration,
Langley Station, Hampton, Va., June 9, 1966.

APPENDIX

CONVERSION OF U.S. CUSTOMARY UNITS TO SI UNITS

The International System of Units (SI) was adopted by the Eleventh General Conference on Weights and Measures, Paris, October 1960. (See ref. 5.) Conversion factors for the physical quantities used in the present investigation are given in the following table:

Physical quantity	U.S. Customary Unit	Conversion factor (*)	SI Unit
Length	in.	0.0254	meters (m)
Temperature	^{o}F	(5/9) (F + 459.67)	degrees Kelvin (^{o}K)
Pressure	lbf/in^2	6894.7572	newtons/meter^2 (N/m^2)
Enthalpy	Btu/lbm	2324.444	joules/kilogram (J/kg) or meters^2/second (m^2/sec^2)
Heat-transfer coefficient	Btu/ft^2-sec-^{o}K	11350	watts/meter^2-^{o}K (W/m^2-^{o}K)
Thermal conductivity	Btu-in./ft^2-sec-^{o}F	518.87315	joules/meter-second-degree Kelvin (J/m-sec-^{o}K)
Heat-transfer rate	Btu/ft^2-sec	11348.931	watts/meter^2 (W/m^2)
Velocity	ft/sec	0.3048	meters/second (m/sec)
Density	lbm/ft^3	16.02	kilograms/meter^3 (kg/m^3)
Viscosity	lbm/ft-sec	1.4881639	newton-seconds/meter^2 ($N\text{-}sec/m^2$)

*Multiply value given in U.S. Customary Unit by conversion factor to obtain value in SI Unit.

Prefixes to indicate multiples of units are as follows:

Prefix	Multiple
mega (M)	10^6
kilo (k)	10^3
centi (c)	10^{-2}
milli (m)	10^{-3}
micro (μ)	10^{-6}

REFERENCES

1. Rainey, Robert W.: Summary of an Advanced Manned Lifting Entry Vehicle Study. NASA TM X-1159, 1965.

2. Harvey, William D.: Pressure Distribution on HL-10 Manned Lifting Entry Vehicle at a Mach Number of 19.5. NASA TM X-1135, 1965.

3. Dunavant, James C.; and Everhart, Philip E.: Investigation of the Heat Transfer to the HL-10 Manned Lifting Entry Vehicle at a Mach Number of 8. NASA TM X-998, 1964.

4. Everhart, Philip E.; and Hamilton, H. Harris: Investigation of Roughness-Induced Turbulent Heating to the HL-10 Manned Lifting Entry Vehicle at a Mach Number of 8. NASA TM X-1101, 1965.

5. Mechtly, E. A.: The International System of Units – Physical Constants and Conversion Factors. NASA SP-7012, 1964.

6. Harvey, William D.: Continuous Skin Construction Technique for Fabricating Models for Aerodynamic Heat-Transfer Studies Involving Very Small Transient Heating Rates. 20th Annual ISA Conference Proceedings, vol. 20, pt. II, paper no. 17.12-7-65, 1965.

7. Miller, Charles G., III; Creel, Theodore R., Jr.; and Smith, Fred M.: Calibration Experience in the Langley Hotshot Tunnel for Mach Numbers from 12 to 26. NASA TN D-3278, 1966.

8. Grabau, Martin; Smithson, H. K., Jr.; and Little, Wanda J.: A Data Reduction Program for Hotshot Tunnels Based on the Fay-Riddell Heat-Transfer Rate Using Nitrogen at Stagnation Temperatures From 1500 to 5000° K. AEDC-TDR-64-50, U.S. Air Force, June 1964.

9. Reshotko, Eli; and Cohen, Clarence B.: Heat Transfer at the Forward Stagnation Point of Blunt Bodies. NACA TN 3513, 1955.

10. Bertram, Mitchel H.; and Everhart, Philip E.: An Experimental Study of the Pressure and Heat-Transfer Distribution on a 70° Sweep Slab Delta Wing in Hypersonic Flow. NASA TR R-153, 1963.

11. Lees, Lester: Laminar Heat Transfer Over Blunt-Nosed Bodies at Hypersonic Flight Speeds. Jet Propulsion, vol. 26, no. 4, Apr. 1956, pp. 259-269, 274.

12. Bertram, Mitchel H.; and Feller, William V.: A Simple Method for Determining Heat Transfer, Skin Friction, and Boundary-Layer Thickness for Hypersonic Laminar Boundary-Layer Flows in a Pressure Gradient. NASA MEMO 5-24-59L, 1959.

13. Harris, Julius E.: Longitudinal Aerodynamic Characteristics of a Manned Lifting Entry Vehicle at a Mach Number of 19.7. NASA TM X-1080, 1965.

TABLE I.- THERMOCOUPLE LOCATIONS

Thermocouple	x/c	s/D_n	Location	Thermocouple	x/c	s/D_n	x_e/c_e	Location
1	-0.375	---	Midline, upper surface	36	0.750	2.42		Leading-edge surface
2	-.188	---	Midline, upper surface	37	.750	2.17		Leading-edge surface
3	-.125	---	Midline, upper surface	38	.750	1.69		Lower surface
4	-.060	---	Midline, upper surface	39	.750	1.33		Lower surface
5	-.030	---	Midline, upper surface	40	.750	.66		Lower surface
6	-.010	---	Midline, upper surface nose	41	.500	---		Upper surface
7	.008	0	Midline, lower surface nose	42	.563	---		Upper surface
8	.030	0	Midline, lower surface	43	.625	---		Upper surface
9	.060	0	Midline, lower surface	44	.688	---		Upper surface
10	.125	0	Midline, lower surface	45	.875	4.00		Tip fin, leading edge
11	.188	0	Midline, lower surface	46	.950	4.30		Tip fin, leading edge
12	.250	0	Midline, lower surface	47	1.000	4.60		Tip fin, leading edge
13	.310	0	Midline, lower surface	48	.950	4.97		Tip fin, inner surface
14	.375	0	Midline, lower surface	49	1.000	5.26		Tip fin, inner surface
15	.500	0	Midline, lower surface	50	.875	3.6		Tip fin, outer surface
16	.625	0	Midline, lower surface	51	.950	3.73		Tip fin, outer surface
17	.750	0	Midline, lower surface	52	1.000	3.94		Tip fin, outer surface
18	.125	2.4	Upper surface	53	.875	3.18		Tip fin, outer surface
19	.125	1.01	Leading-edge surface	54	.950	3.23		Tip fin, outer surface
20	.125	.53	Leading-edge surface	55	.950	2.43		Tip fin, outer surface
21	.125	.2	Lower surface	56	.907	1.867	0.245	Elevon, upper surface
22	.250	2.27	Upper surface	57	.938	1.867	.497	Elevon, upper surface
23	.250	1.8	Upper surface	58	.970	1.867	.748	Elevon, upper surface
24	.250	1.15	Leading-edge surface	59	.918	1.267	.230	Elevon, upper surface
25	.250	.89	Leading-edge surface	60	.945	1.267	.486	Elevon, upper surface
26	.250	.67	Leading-edge surface	61	.974	1.267	.744	Elevon, upper surface
27	.500	3.03	Upper surface	62	.925	1.12	.270	Elevon, lower surface
28	.500	2.6	Upper surface	63	.950	1.12	.514	Elevon, lower surface
29	.500	2.16	Leading-edge surface	64	.975	1.12	.757	Elevon, lower surface
30	.500	1.9	Leading-edge surface	65	.914	1.573	.254	Elevon, lower surface
31	.500	.135	Lower surface	66	.943	1.573	.502	Elevon, lower surface
32	.500	.66	Lower surface	67	.971	1.573	.752	Elevon, lower surface
33	.750	3.33	Upper surface	68	.903	2.027	.241	Elevon, lower surface
34	.750	2.95	Upper surface	69	.935	2.027	.494	Elevon, lower surface
35	.750	2.66	Leading-edge surface	70	.968	2.027	.747	Elevon, lower surface

TABLE II.- ORDINATES DEFINING CROSS-SECTIONAL SHAPE OF HL-10 MODEL WITHOUT TIP FINS

z/c	y/c
x/c = 0.042	
0.0541	0
.0532	.0083
.0503	.0167
.0441	.0250
.0375	.0306
.0333	.0338
.0250	.0390
.0167	.0431
.0083	.0459
0	.0476
-.0536	0
x/c = 0.083	
0.0681	0
.0668	.0083
.0637	.0167
.0579	.0250
.0502	.0333
.0417	.0392
.0330	.0444
.0250	.0487
.0167	.0521
.0083	.0547
0	.0568
-.0083	.0585
-.0167	.0596
-.0752	0
x/c = 0.125	
0.0737	0
.0729	.0083
.0702	.0167
.0660	.0250
.0594	.0330
.0505	.0417
.0417	.0477
.0333	.0528
.0250	.0571
.0167	.0604
.0083	.0632
0	.0656
-.0083	.0675
-.0167	.0691
-.0250	.0704
-.0333	.0714
-.0904	0
x/c = 0.167	
0.0771	0
.0763	.0083
.0744	.0167
.0712	.0250
.0664	.0333
.0597	.0417
.0512	.0500
.0417	.0565
.0333	.0618
.0250	.0664
.0167	.0701
.0083	.0732
0	.0757
-.0083	.0778
-.0167	.0796
-.0250	.0811
-.0333	.0823
-.0417	.0833
-.0500	.0840
-.1026	0

z/c	y/c
x/c = 0.208	
0.0792	0
.0787	.0083
.0772	.0167
.0747	.0250
.0712	.0333
.0664	.0416
.0592	.0500
.0517	.0583
.0417	.0656
.0333	.0713
.0250	.0760
.0167	.0800
.0083	.0833
0	.0860
-.0083	.0882
-.0167	.0902
-.0250	.0919
-.0333	.0933
-.0417	.0946
-.0500	.0955
-.0583	.0962
-.1126	0
x/c = 0.250	
0.0807	0
.0803	.0083
.0792	.0167
.0773	.0250
.0748	.0333
.0712	.0417
.0666	.0500
.0606	.0583
.0527	.0667
.0458	.0721
.0417	.0754
.0333	.0811
.0250	.0862
.0167	.0902
.0083	.0937
0	.0965
-.0083	.0990
-.0167	.1011
-.0250	.1027
-.0333	.1044
-.0417	.1057
-.0500	.1067
-.0583	.1076
-.0667	.1083
-.1205	0
x/c = 0.292	
0.0817	0
.0814	.0083
.0807	.0167
.0794	.0250
.0774	.0333
.0750	.0417
.0715	.0500
.0672	.0583
.0617	.0667
.0546	.0750
.0500	.0789
.0417	.0858
.0333	.0918
.0250	.0969
.0167	.1010
.0083	.1044
0	.1072
-.0083	.1098
-.0167	.1119

z/c	y/c
x/c = 0.292 Concluded	
-0.0250	0.1137
-.0333	.1156
-.0417	.1170
-.0500	.1182
-.0583	.1192
-.0667	.1198
-.0750	.1202
-.1268	0
x/c = 0.333	
0.0820	0
.0818	.0083
.0813	.0167
.0803	.0250
.0789	.0333
.0771	.0417
.0747	.0500
.0716	.0583
.0677	.0667
.0627	.0750
.0564	.0833
.0485	.0917
.0417	.0968
.0333	.1027
.0250	.1078
.0167	.1119
.0083	.1152
0	.1179
-.0083	.1204
-.0167	.1227
-.0250	.1250
-.0333	.1267
-.0417	.1282
-.0500	.1296
-.0583	.1306
-.0667	.1317
-.0750	.1321
-.1312	0
x/c = 0.375	
0.0821	0
.0820	.0083
.0816	.0167
.0809	.0250
.0799	.0333
.0783	.0417
.0766	.0500
.0744	.0583
.0714	.0667
.0679	.0750
.0633	.0833
.0576	.0917
.0503	.1000
.0415	.1083
.0333	.1136
.0250	.1187
.0167	.1229
.0083	.1262
0	.1292
-.0083	.1315
-.0167	.1337
-.0250	.1358
-.0333	.1377
-.0417	.1394
-.0500	.1408
-.0583	.1420
-.0667	.1429
-.0750	.1437
-.0833	.1422
-.1334	0

z/c	y/c
x/c = 0.417	
0.0814	0
.0813	.0083
.0811	.0167
.0805	.0250
.0797	.0333
.0786	.0417
.0772	.0500
.0755	.0583
.0733	.0667
.0706	.0750
.0674	.0833
.0633	.0917
.0582	.1000
.0517	.1083
.0437	.1167
.0375	.1211
.0333	.1241
.0250	.1296
.0167	.1339
.0083	.1375
0	.1406
-.0083	.1431
-.0167	.1453
-.0250	.1472
-.0333	.1492
-.0417	.1508
-.0500	.1523
-.0583	.1536
-.0667	.1546
-.0750	.1554
-.0833	.1559
-.1340	0
x/c = 0.458	
0.0800	0
.0799	.0083
.0797	.0167
.0794	.0250
.0788	.0333
.0780	.0417
.0768	.0500
.0755	.0583
.0739	.0667
.0720	.0750
.0694	.0833
.0664	.0917
.0629	.1000
.0581	.1083
.0526	.1167
.0453	.1250
.0363	.1333
.0292	.1379
.0250	.1407
.0167	.1454
.0083	.1491
0	.1521
-.0083	.1549
-.0167	.1571
-.0250	.1592
-.0333	.1611
-.0417	.1627
-.0500	.1642
-.0583	.1654
-.0667	.1664
-.0750	.1672
-.0833	.1677
-.1322	0

z/c	y/c
x/c = 0.500	
0.0782	0
.0782	.0167
.0780	.0250
.0776	.0333
.0770	.0417
.0762	.0500
.0751	.0583
.0738	.0667
.0723	.0750
.0705	.0833
.0682	.0917
.0655	.1000
.0620	.1083
.0579	.1167
.0529	.1250
.0467	.1333
.0390	.1417
.0333	.1458
.0250	.1521
.0167	.1571
.0083	.1612
0	.1643
-.0083	.1672
-.0167	.1694
-.0250	.1715
-.0333	.1733
-.0417	.1750
-.0500	.1763
-.0583	.1775
-.0667	.1785
-.0750	.1792
-.1285	0
x/c = 0.542	
0.0759	0
.0759	.0166
.0758	.0249
.0756	.0332
.0752	.0415
.0747	.0498
.0740	.0581
.0730	.0664
.0718	.0747
.0705	.0830
.0688	.0913
.0666	.0996
.0642	.1079
.0611	.1162
.0575	.1245
.0530	.1328
.0476	.1411
.0410	.1494
.0326	.1577
.0249	.1629
.0166	.1685
.0083	.1729
0	.1764
-.0083	.1790
-.0166	.1815
-.0249	.1834
-.0332	.1853
-.0415	.1869
-.0498	.1882
-.0581	.1893
-.0664	.1902
-.1229	0

z/c	y/c
x/c = 0.583	
0.0741	0
.0741	.0104
.0740	.0271
.0735	.0437
.0726	.0604
.0710	.0771
.0671	.0937
.0668	.1020
.0651	.1104
.0626	.1187
.0596	.1270
.0563	.1354
.0521	.1437
.0471	.1520
.0412	.1604
.0337	.1687
.0250	.1756
.0167	.1813
.0083	.1860
0	.1897
-.0083	.1926
-.0167	.1949
-.0250	.1970
-.0333	.1988
-.0417	.2003
-.0500	.2017
-.0583	.2028
-.1156	0
x/c = 0.625	
0.0716	0
.0716	.0104
.0716	.0271
.0713	.0437
.0707	.0604
.0696	.0771
.0678	.0937
.0655	.1104
.0637	.1187
.0616	.1270
.0591	.1354
.0558	.1437
.0521	.1520
.0478	.1604
.0429	.1687
.0365	.1770
.0292	.1842
.0250	.1878
.0167	.1941
.0083	.1991
0	.2028
-.0083	.2057
-.0167	.2080
-.0250	.2101
-.0333	.2118
-.0417	.2132
-.0500	.2143
-.1073	0
x/c = 0.667	
0.0667	0
.0686	.0208
.0686	.0375
.0684	.0541
.0678	.0708
.0669	.0875
.0655	.1041
.0634	.1208
.0601	.1374
.0580	.1458

z/c	y/c
x/c = 0.667 Concluded	
0.0553	0.1541
.0522	.1624
.0483	.1708
.0439	.1791
.0385	.1874
.0317	.1958
.0250	.2015
.0167	.2080
.0083	.2128
0	.2167
-.0083	.2197
-.0167	.2218
-.0250	.2237
-.0333	.2254
-.0417	.2264
-.0986	0
x/c = 0.708	
0.0654	0
.0653	.0417
.0651	.0583
.0650	.0750
.0643	.0916
.0634	.1083
.0617	.1250
.0596	.1416
.0582	.1499
.0563	.1583
.0542	.1666
.0517	.1749
.0487	.1833
.0446	.1916
.0398	.1999
.0340	.2083
.0292	.2130
.0250	.2168
.0167	.2235
.0083	.2283
0	.2317
-.0083	.2343
-.0167	.2363
-.0250	.2378
-.0333	.2390
-.0889	0
x/c = 0.750	
0.0617	0
.0616	.0625
.0615	.0791
.0611	.0958
.0606	.1125
.0596	.1291
.0581	.1458
.0561	.1624
.0533	.1791
.0488	.1958
.0458	.2041
.0421	.2124
.0372	.2207
.0333	.2256
.0292	.2307
.0250	.2347
.0167	.2409
.0083	.2447
0	.2470
-.0083	.2491
-.0167	.2504
-.0250	.2511
-.0785	0

z/c	y/c
x/c = 0.792	
0.0578	0
.0577	.0937
.0576	.1104
.0573	.1270
.0569	.1437
.0561	.1604
.0549	.1770
.0532	.1937
.0506	.2103
.0486	.2187
.0460	.2270
.0425	.2353
.0375	.2437
.0333	.2481
.0250	.2551
.0167	.2588
.0083	.2611
0	.2624
-.0083	.2631
-.0167	.2634
-.0673	0
x/c = 0.833	
0.0536	0
.0534	.1666
.0532	.1833
.0528	.1999
.0521	.2166
.0510	.2332
.0482	.2499
.0455	.2582
.0400	.2666
.0333	.2707
.0250	.2736
.0167	.2749
.0083	.2753
0	.2753
-.0563	0
x/c = 0.875	
0.0487	0
-.0452	0
x/c = 0.917	
0.0440	0
-.0341	0
x/c = 0.958	
0.0392	0
-.0227	0
x/c = 1.000	
0.0344	0
-.0125	0

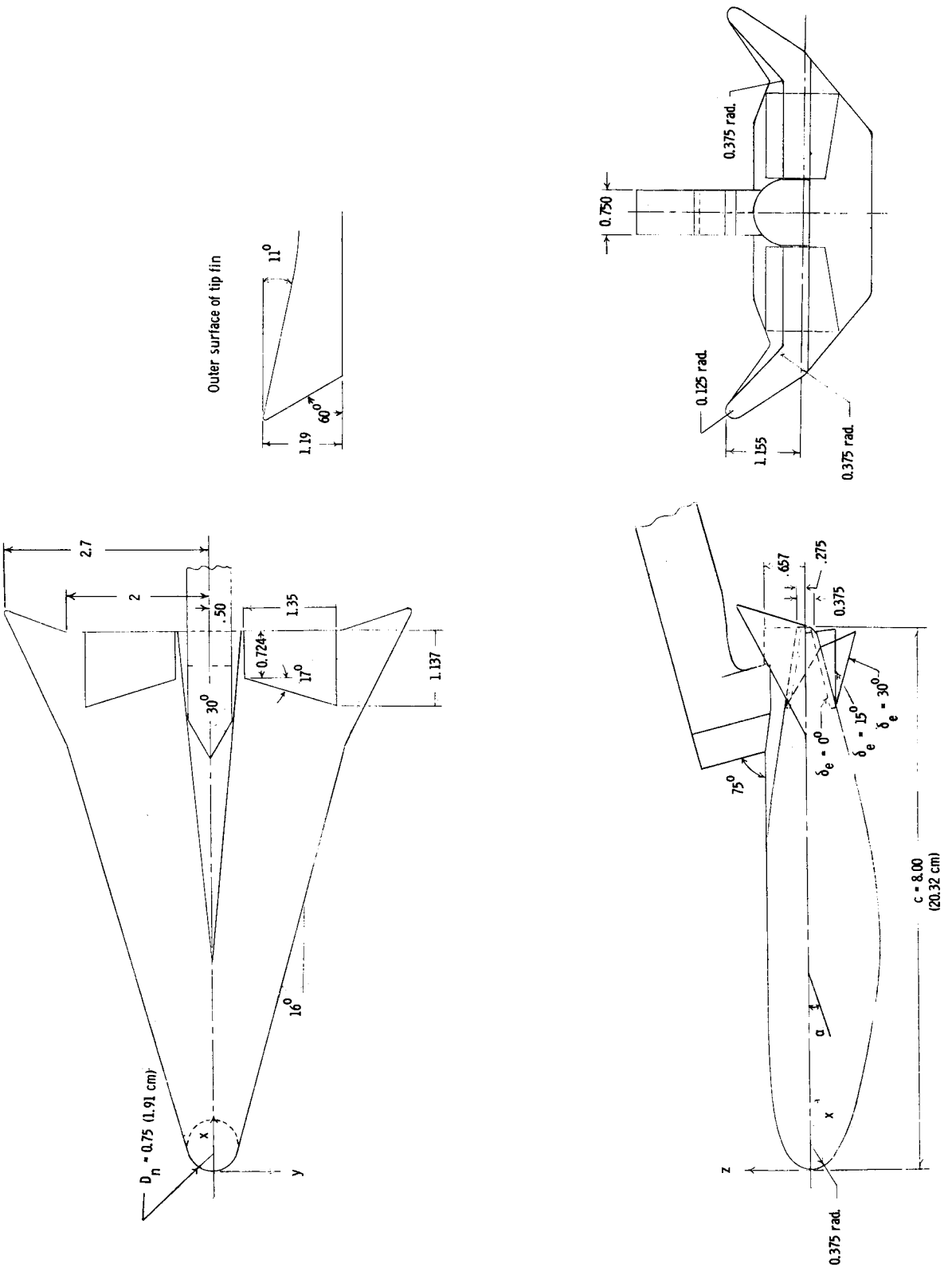

Figure 1.- Drawing of 8-inch HL-10 model. Dimensions are in inches unless otherwise noted. Because of space limitations, conversions to the International System of Units are presented for only a few representative dimensions.

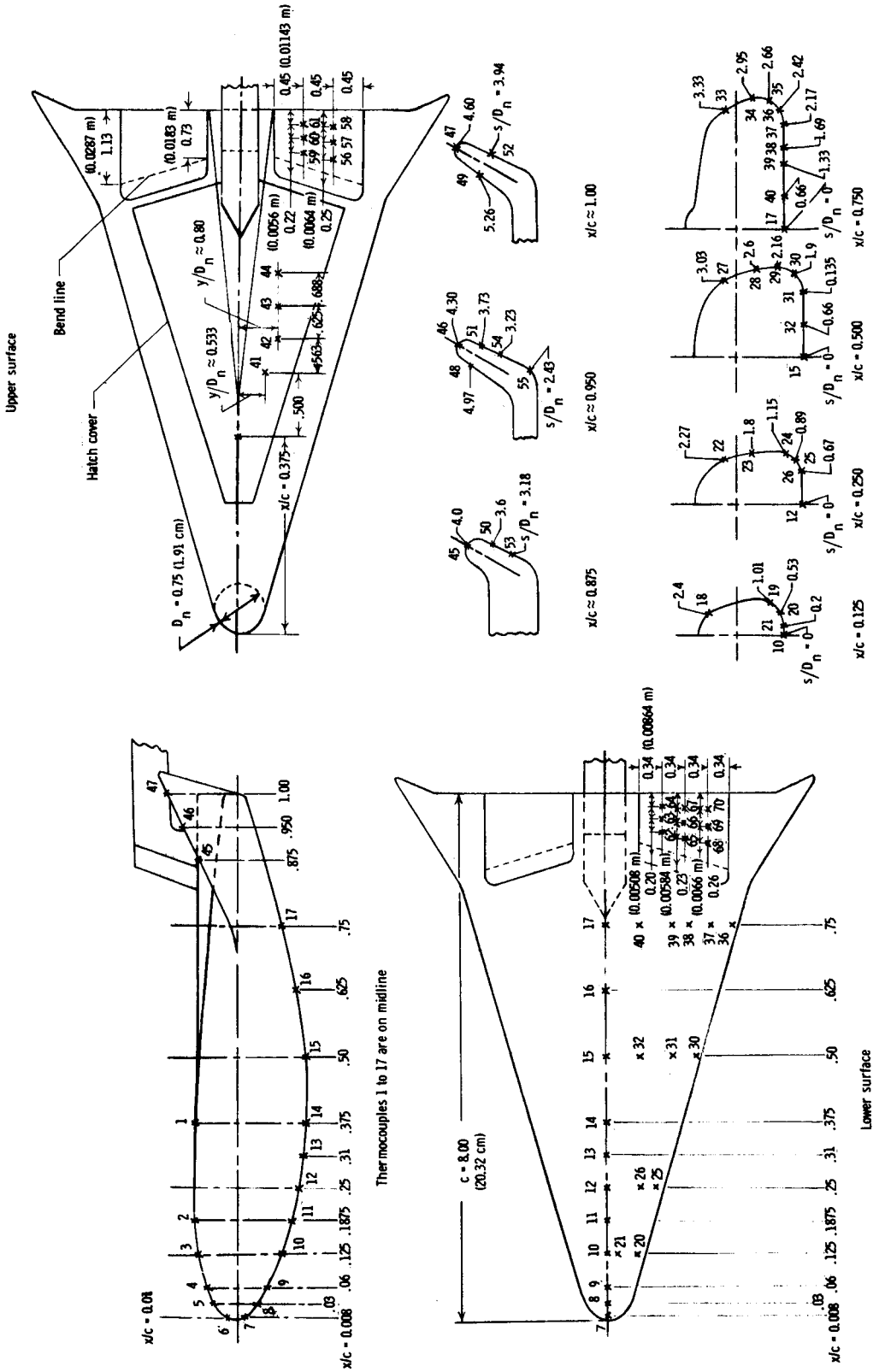

Figure 2.- Thermocouple locations on HL-10 heat-transfer model. Dimensions are in inches unless otherwise noted.

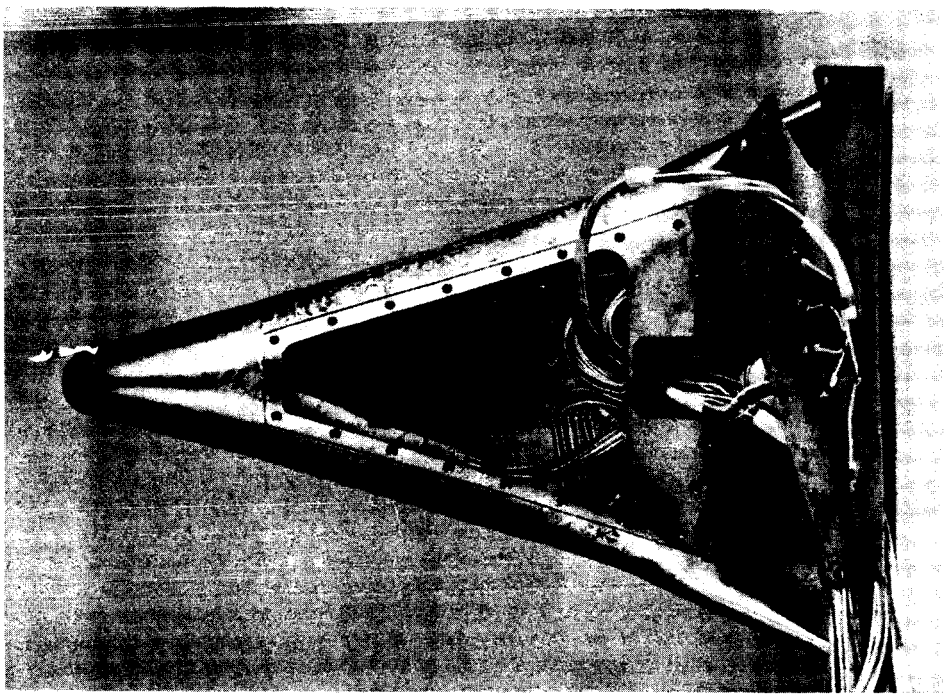

(a) Top view. Hatch cover off.

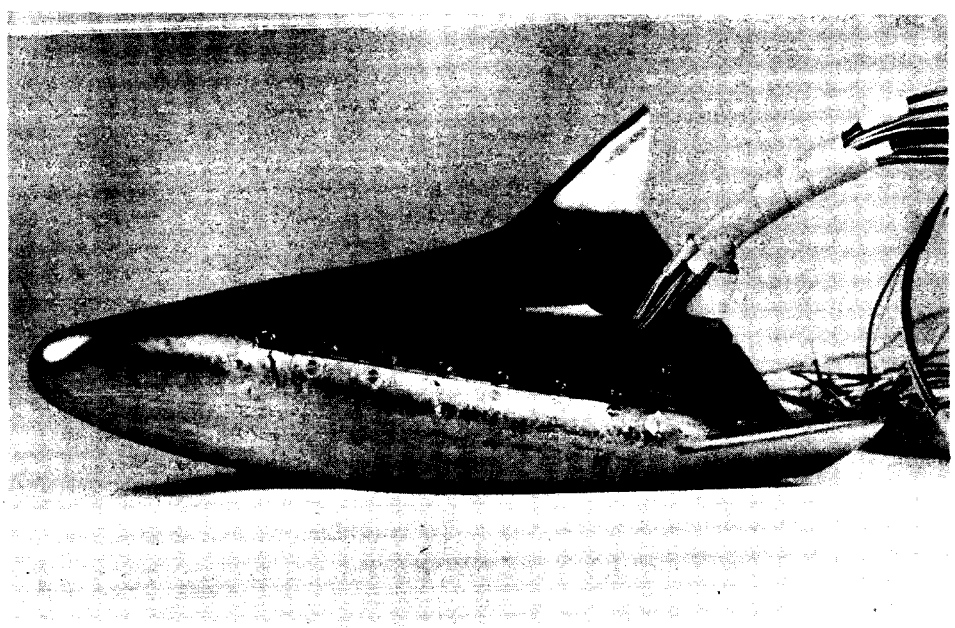

(b) Side view. Hatch cover on.

Figure 3.- Photographs of HL-10 heat-transfer model.

L-66-4468

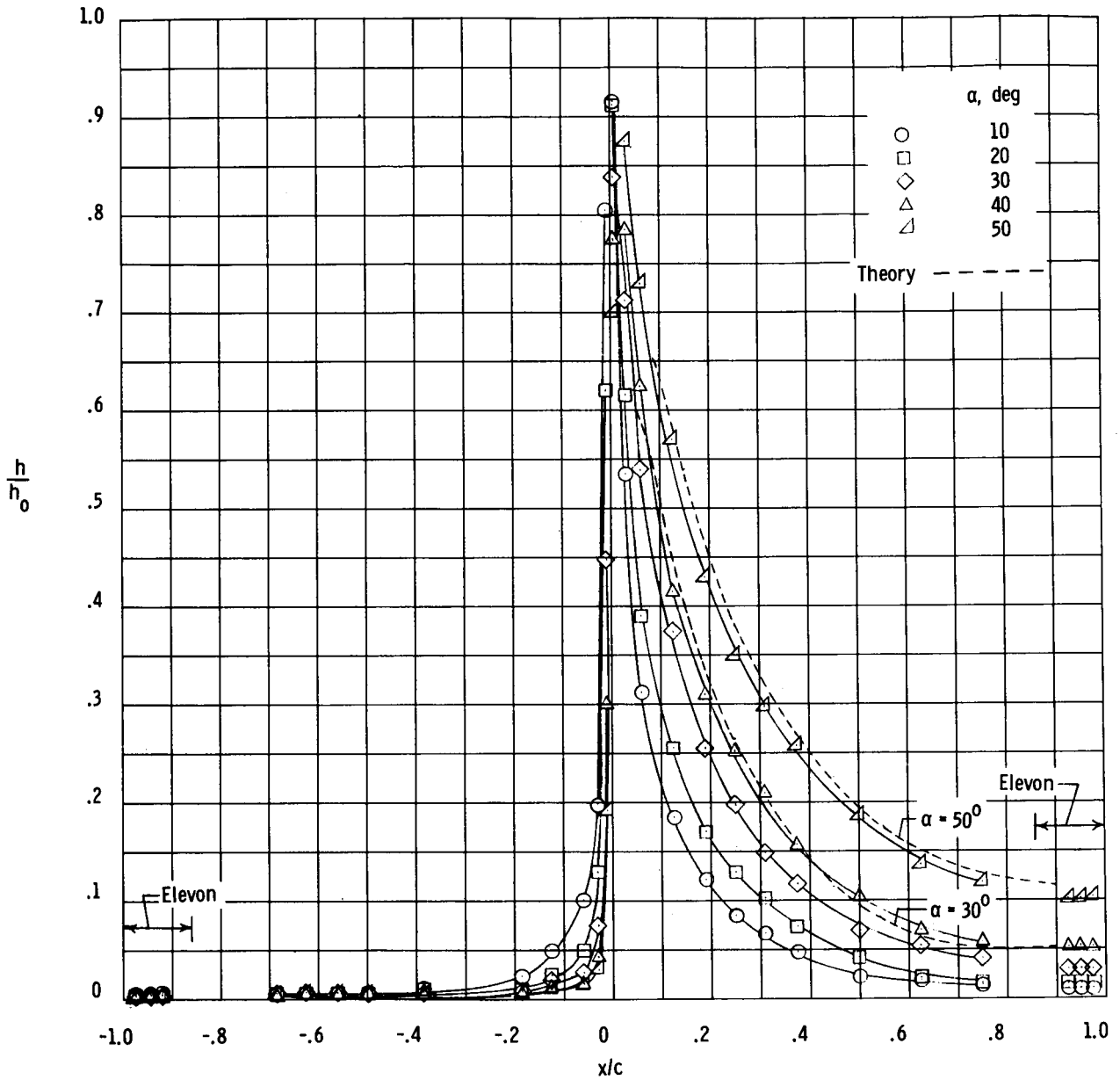

Figure 4.- Heat-transfer distribution along midline for angles of attack from 10^0 to 50^0. $\delta_e = 0^0$.

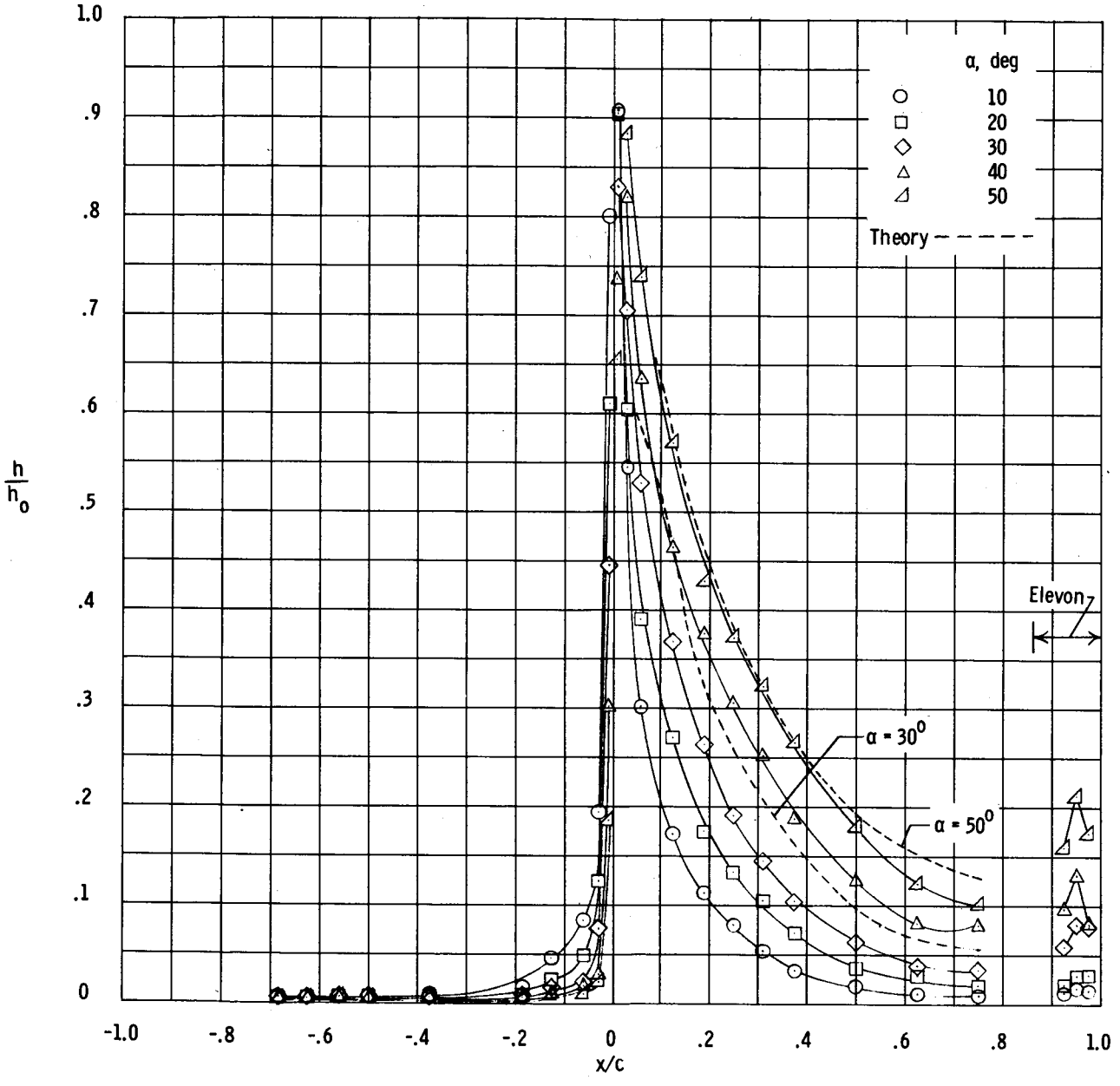

Figure 5.- Heat-transfer distribution along midline for angles of attack from 10° to 50°. $\delta_e = 15°$.

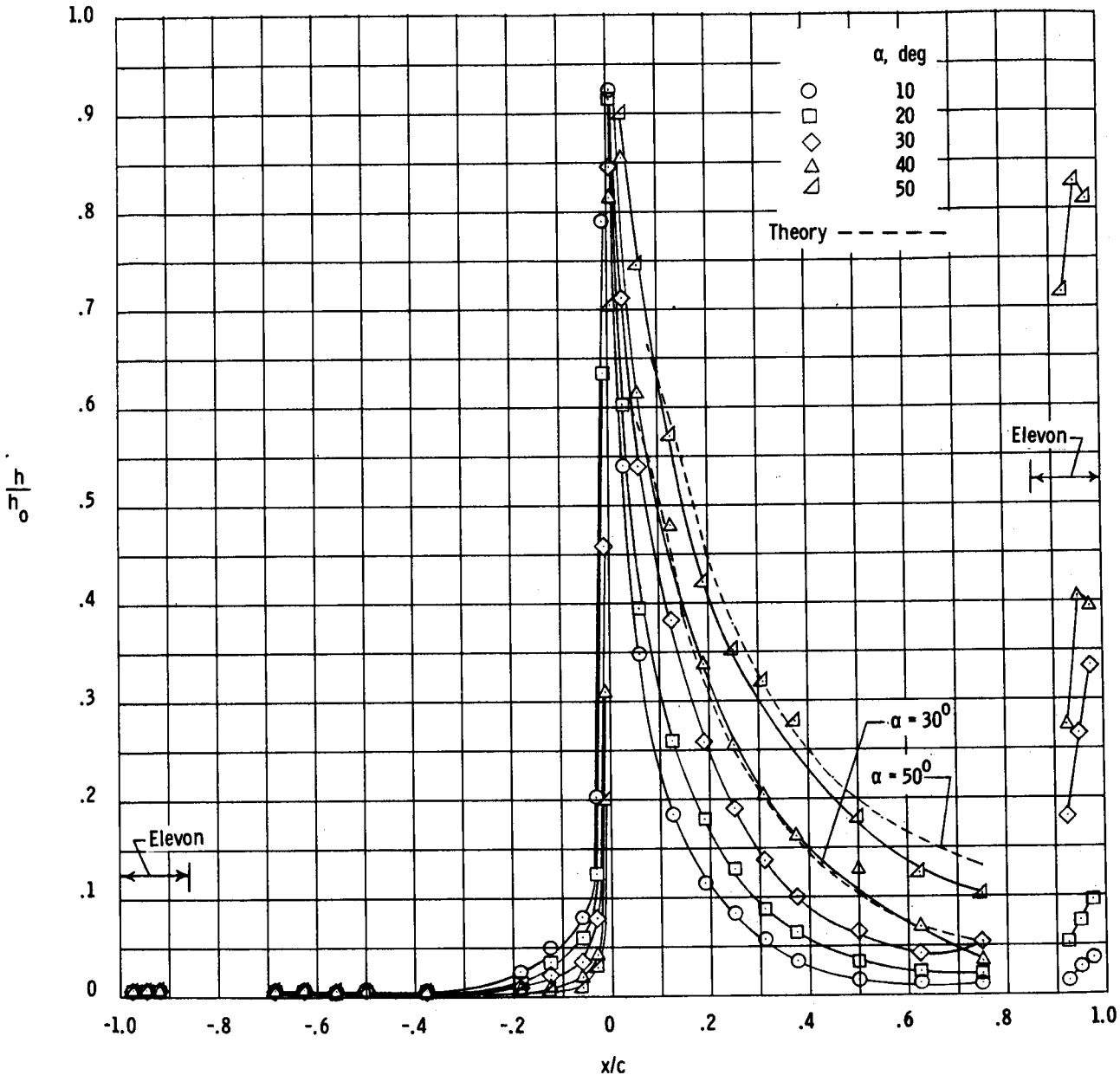

Figure 6.- Heat-transfer distribution along midline for angles of attack from 10^0 to 50^0. $\delta_e = 30^0$.

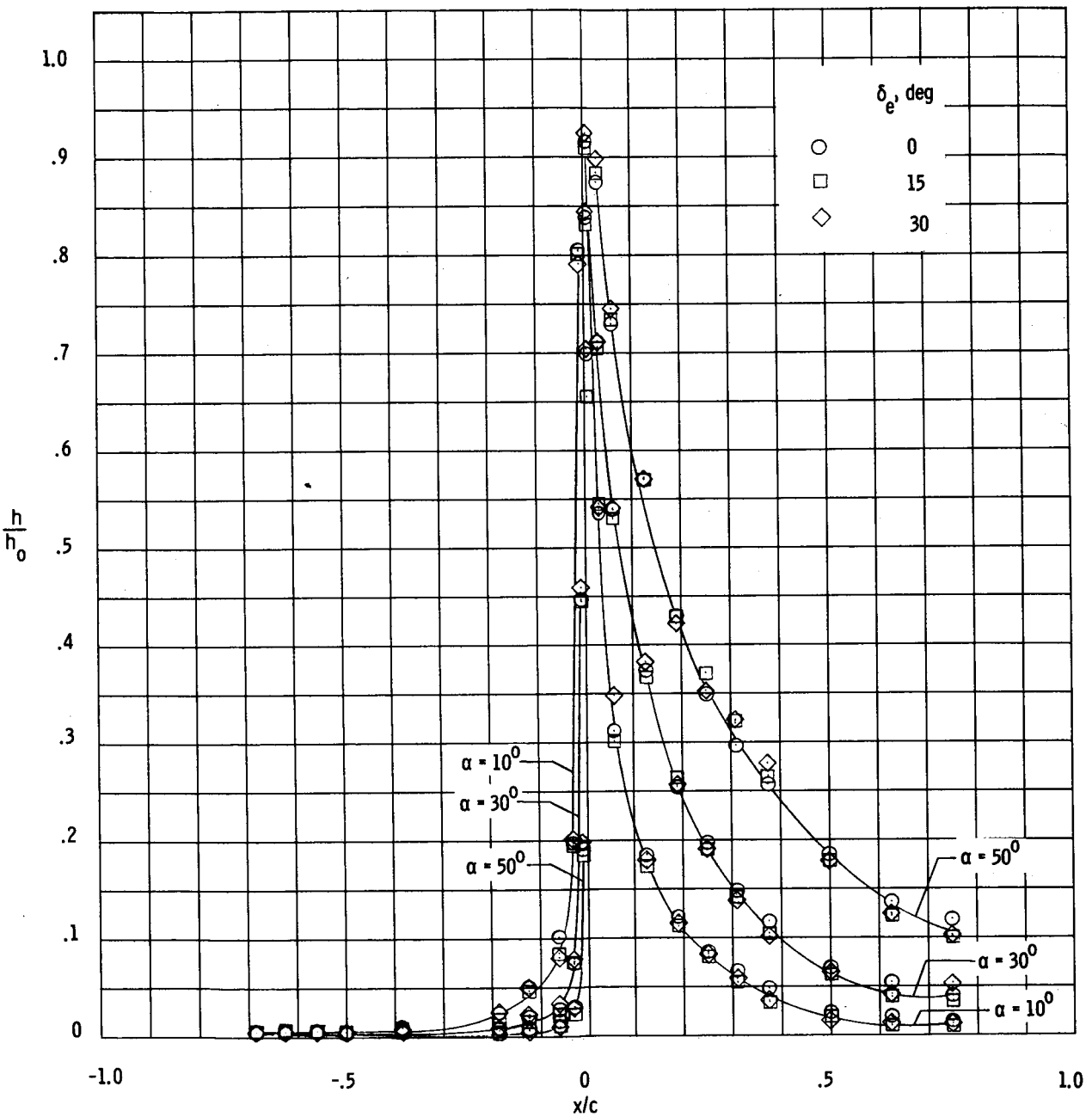

Figure 7.- Summary of heat-transfer distribution along midline for three angles of attack.

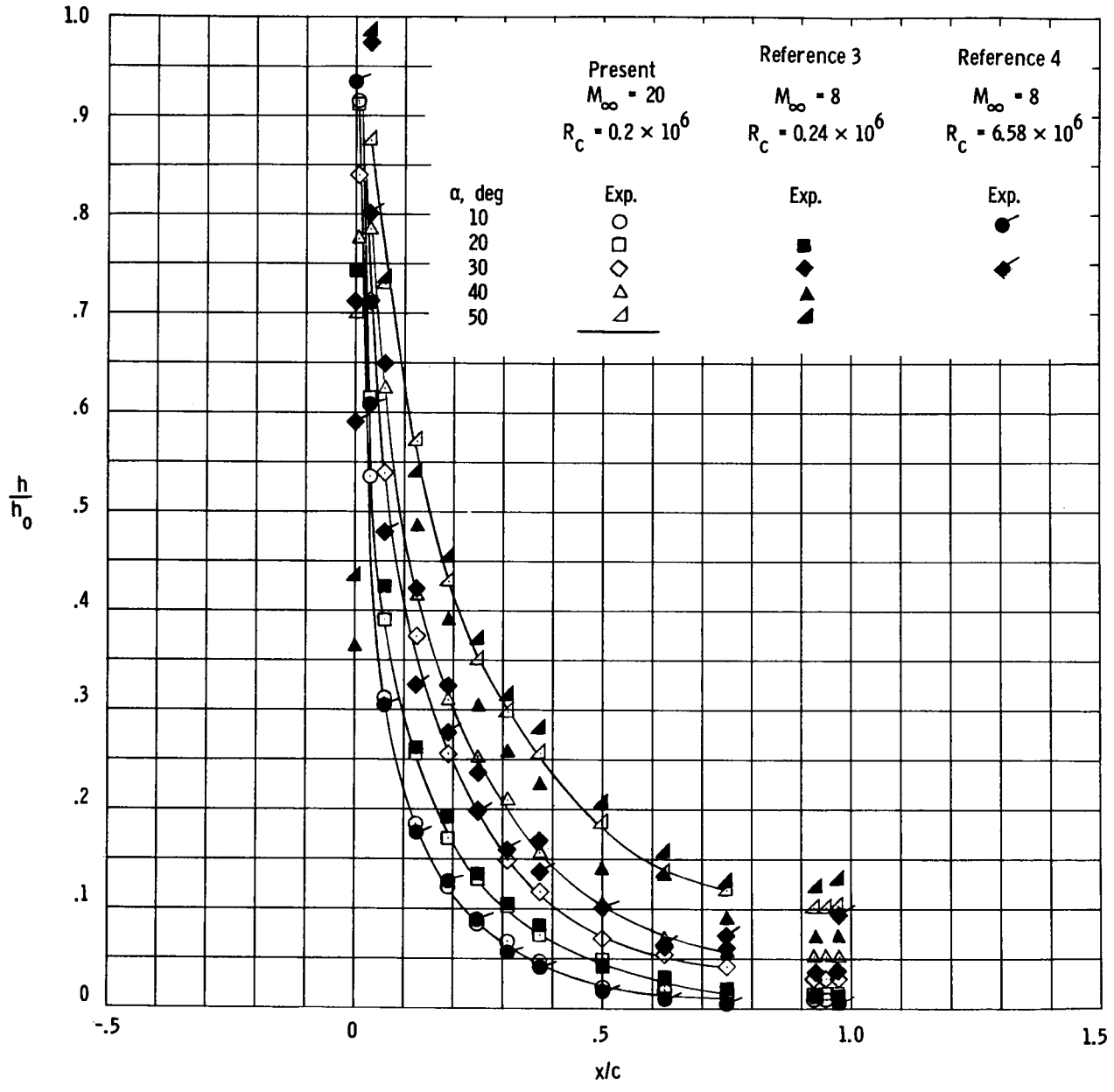

Figure 8.- Comparison of present heat-transfer distribution along lower-surface midline with Mach 8 results for angles of attack from 10^0 to 50^0. $\delta_e = 0^0$.

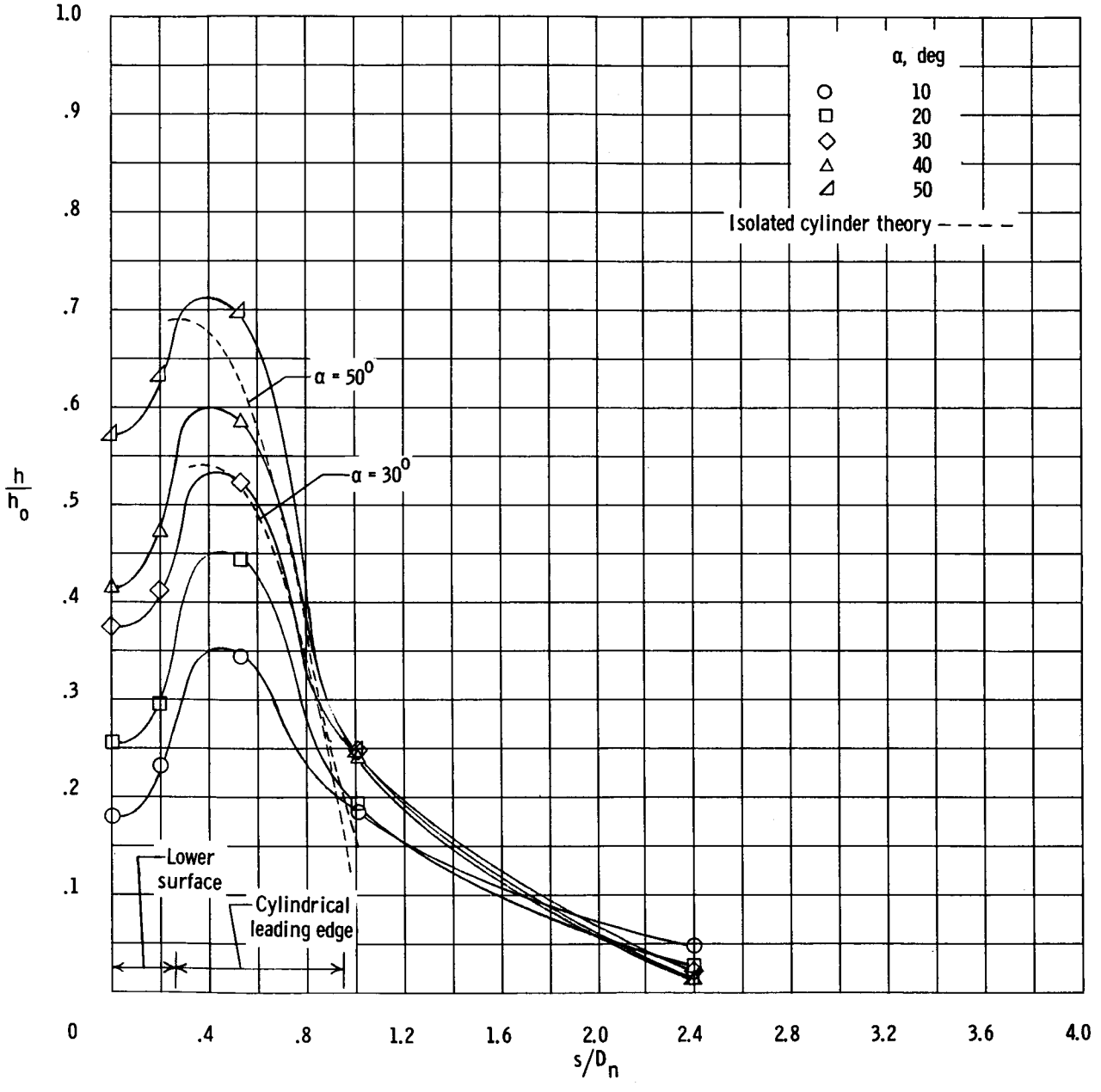

(a) x/c = 0.125.

Figure 9.- Spanwise heat-transfer distribution for various chordwise stations for angles of attack from 10° to 50°. $\delta_e = 0°$.

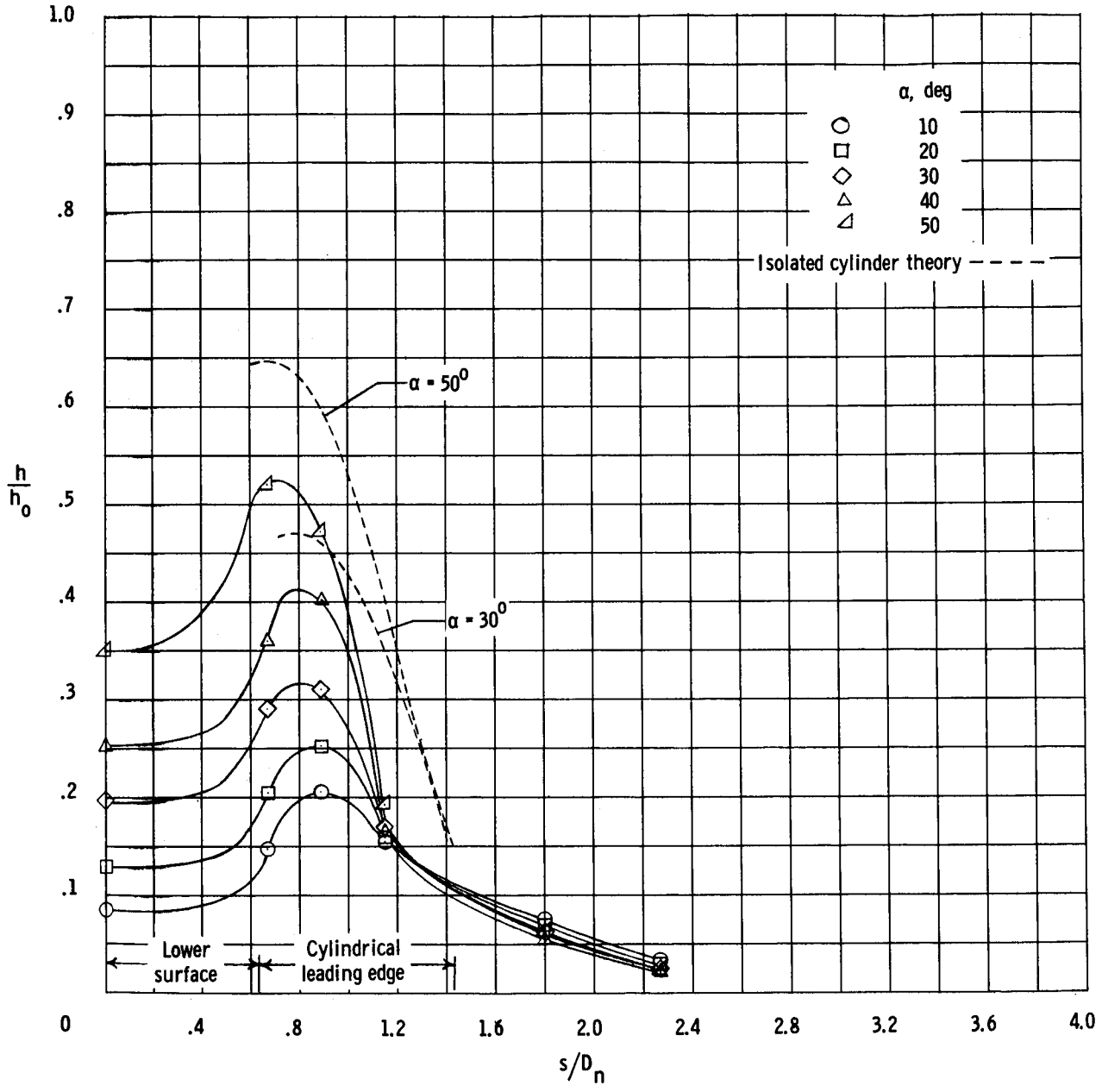

(b) x/c = 0.250.

Figure 9.- Continued.

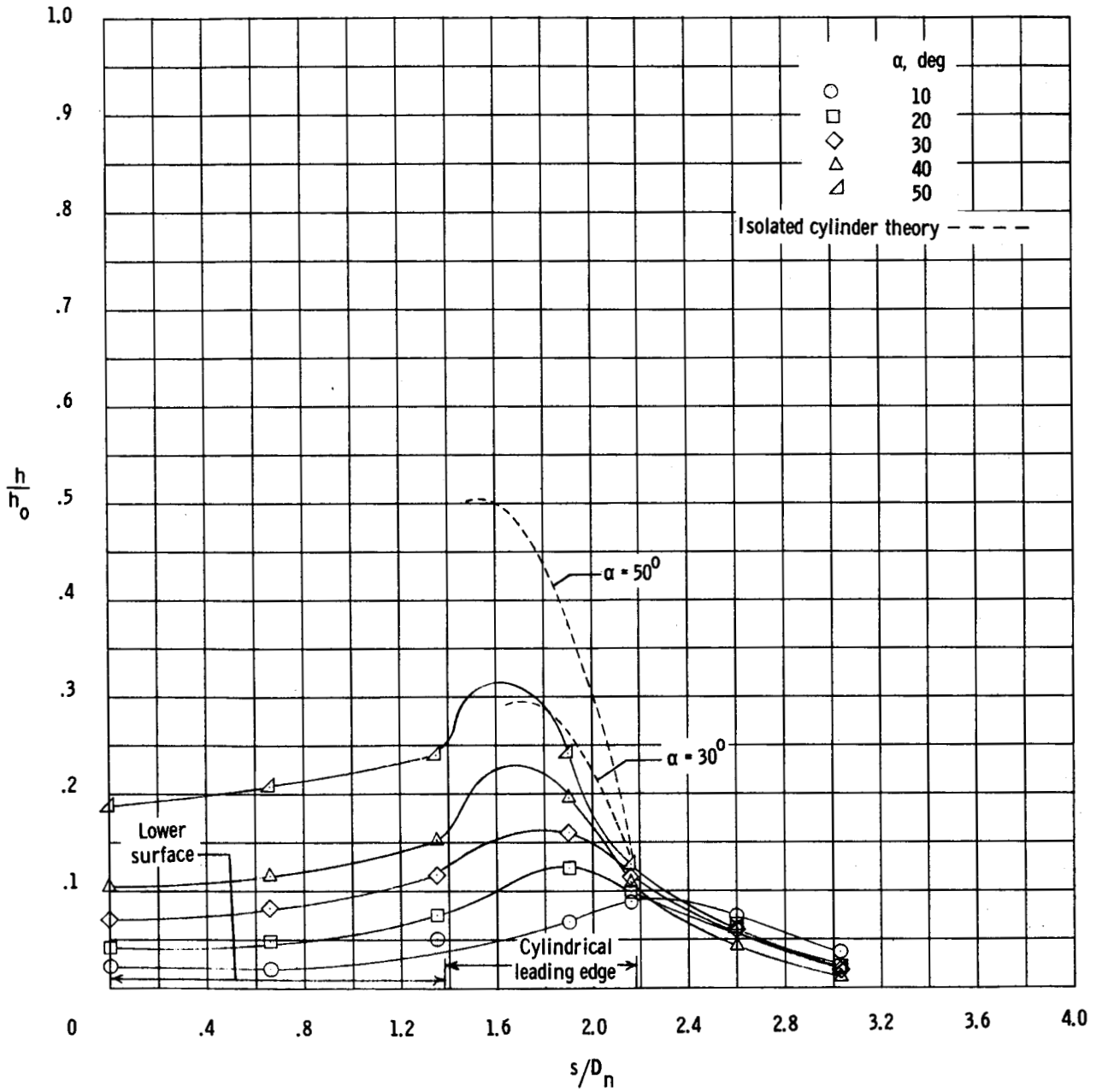

(c) x/c = 0.500.

Figure 9.- Continued.

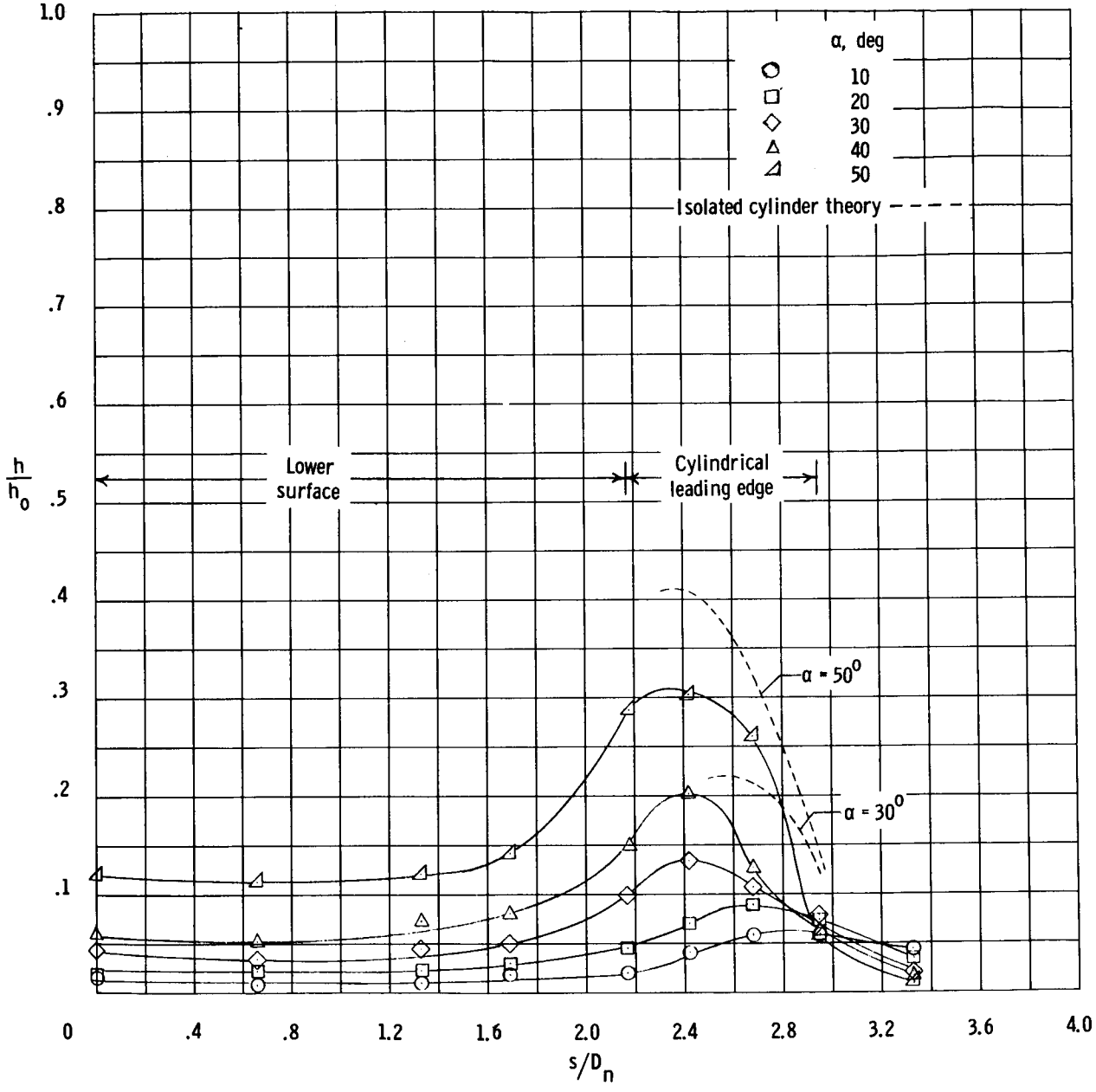

(d) x/c = 0.750.

Figure 9.- Continued.

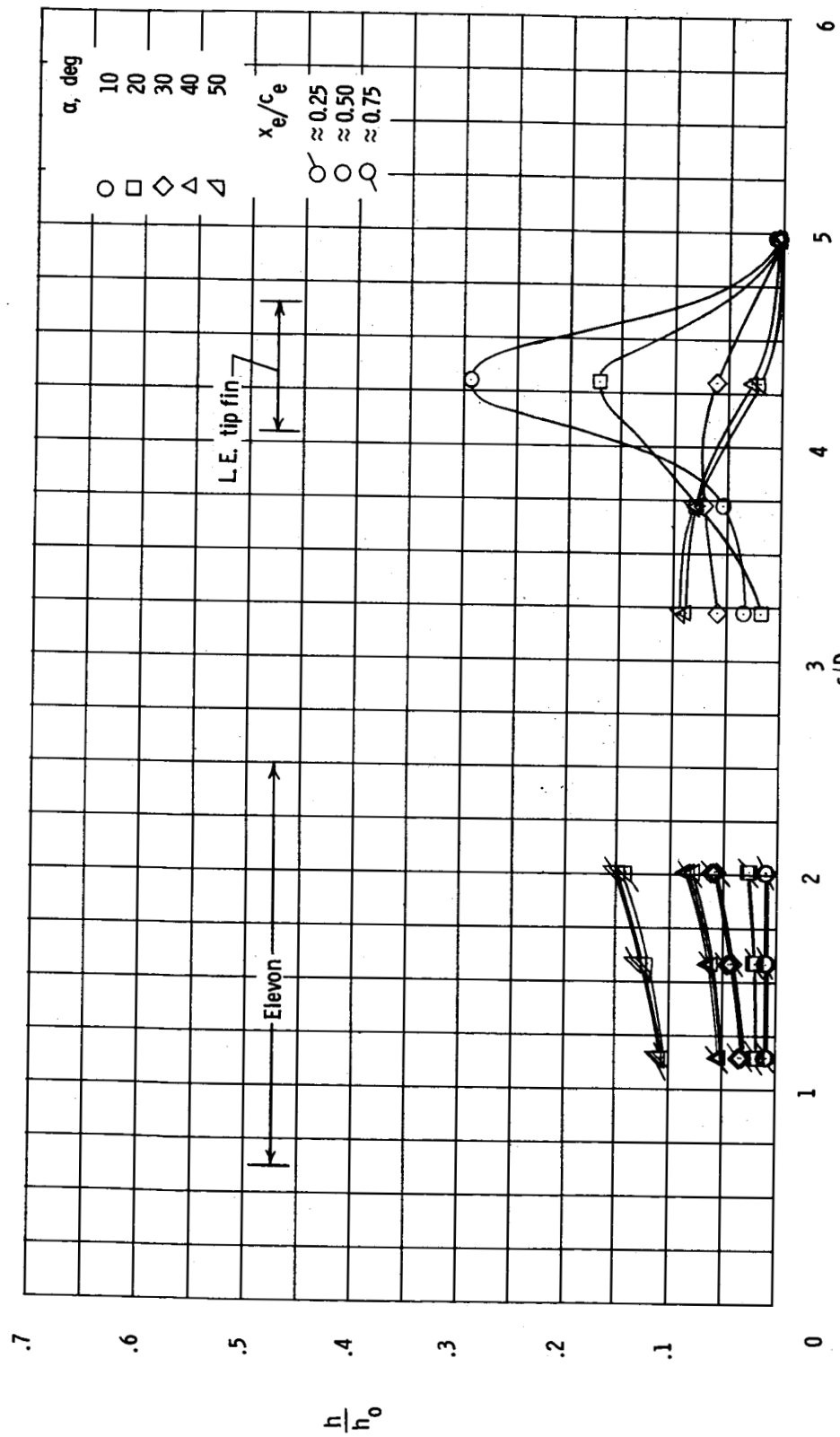

(e) $x/c \approx 0.950$.

Figure 9.- Concluded.

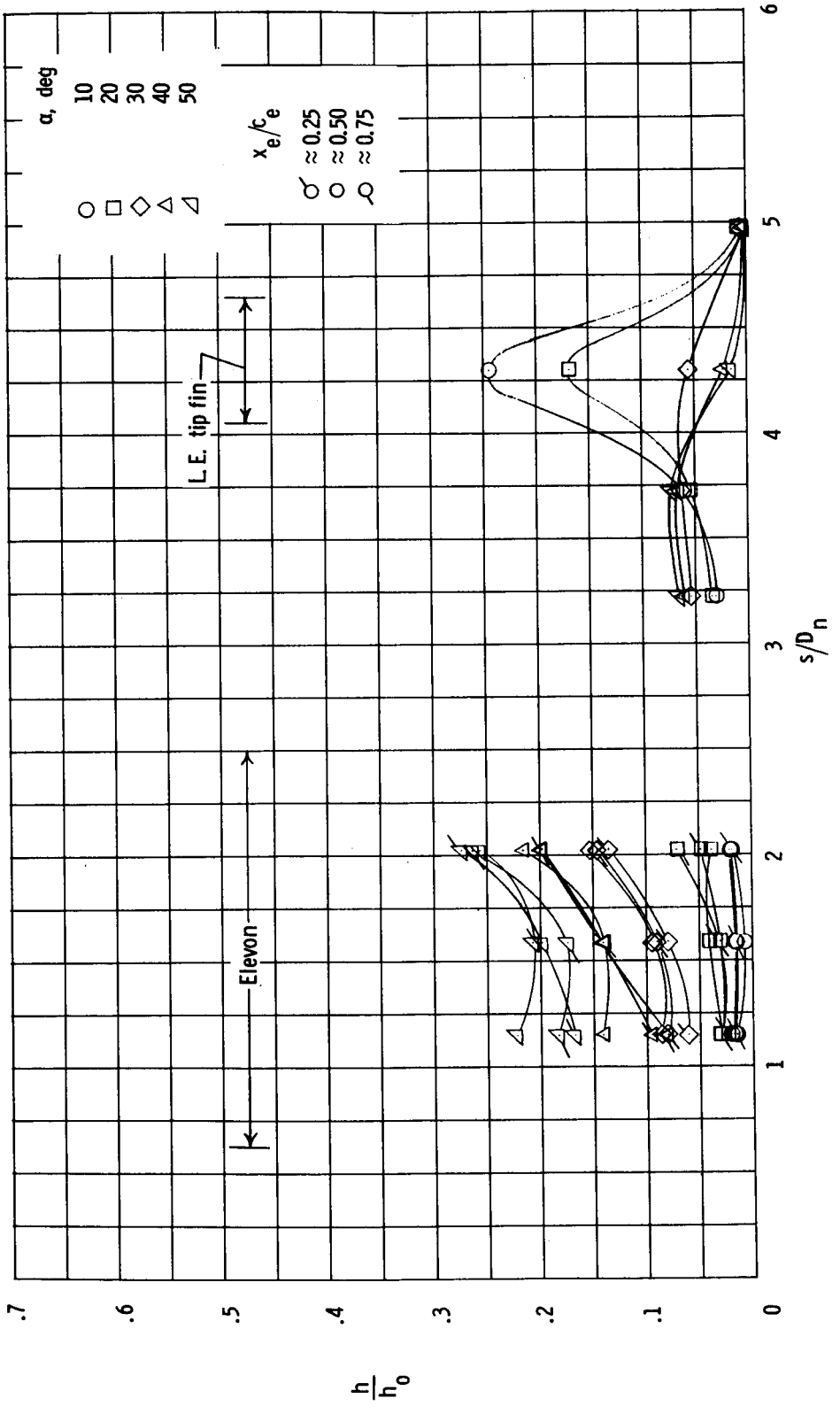

Figure 10.- Spanwise heat-transfer distribution at station $x/c \approx 0.950$ for angles of attack. $\delta_e = 15^0$.

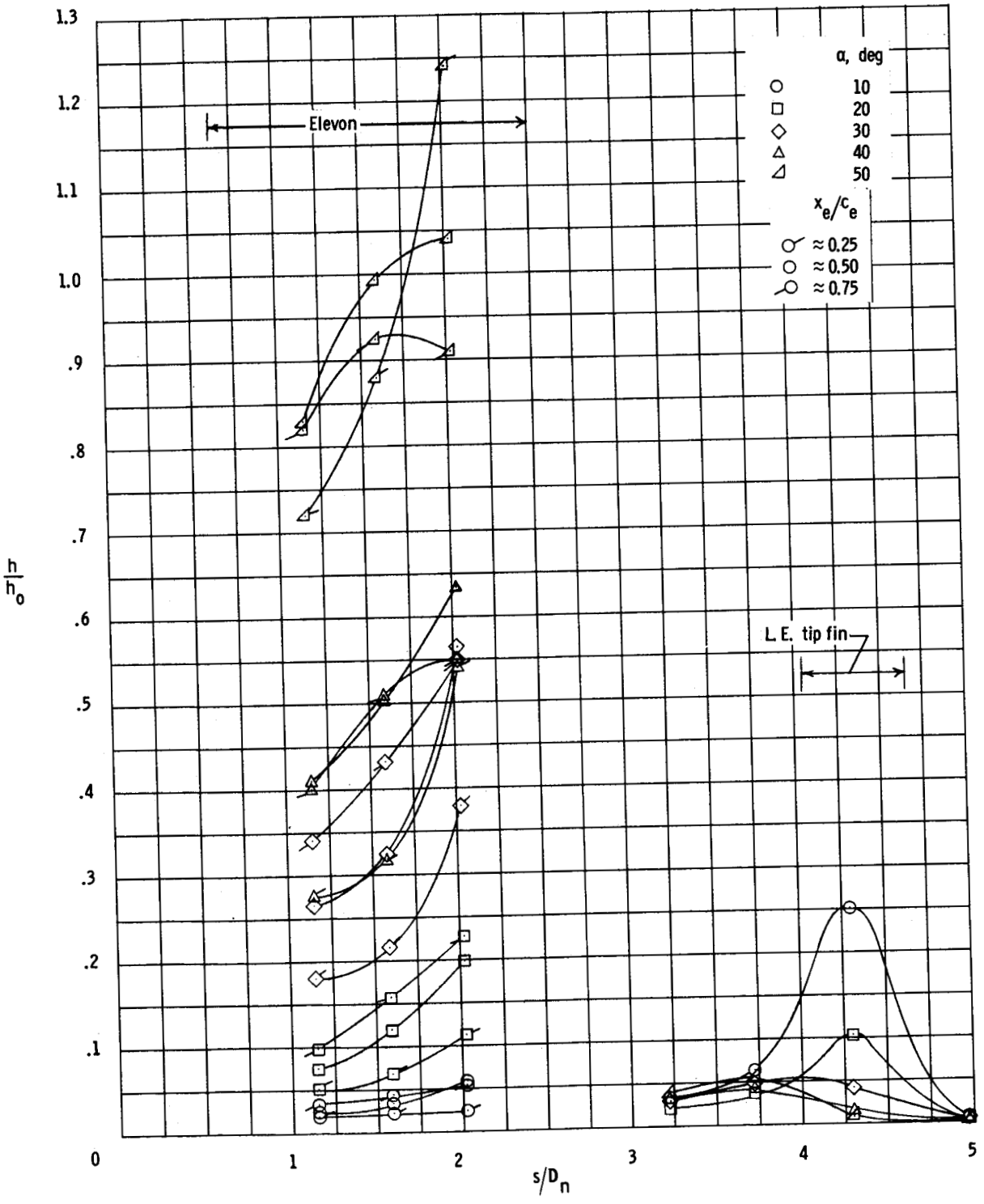

Figure 11.- Spanwise heat-transfer distribution at $x/c \approx 0.950$ for angles of attack. $\delta_e = 30^0$.

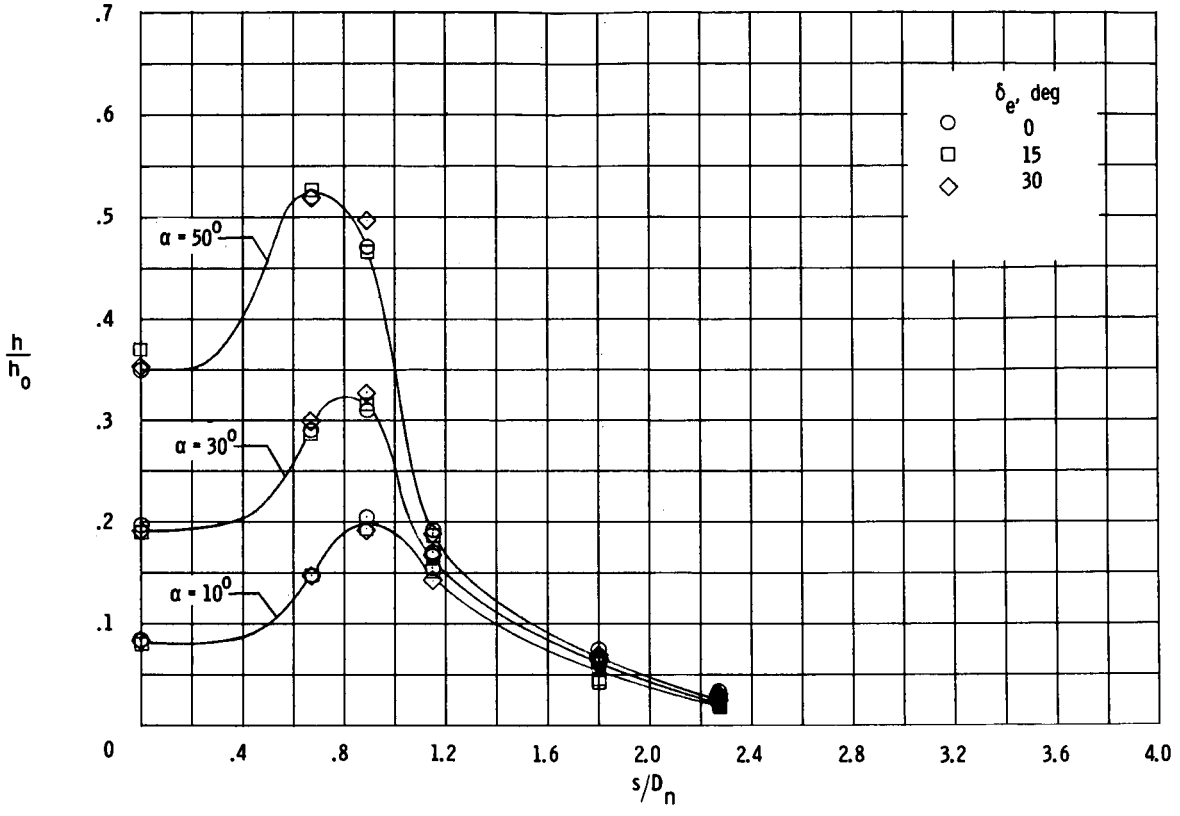

(a) x/c = 0.250.

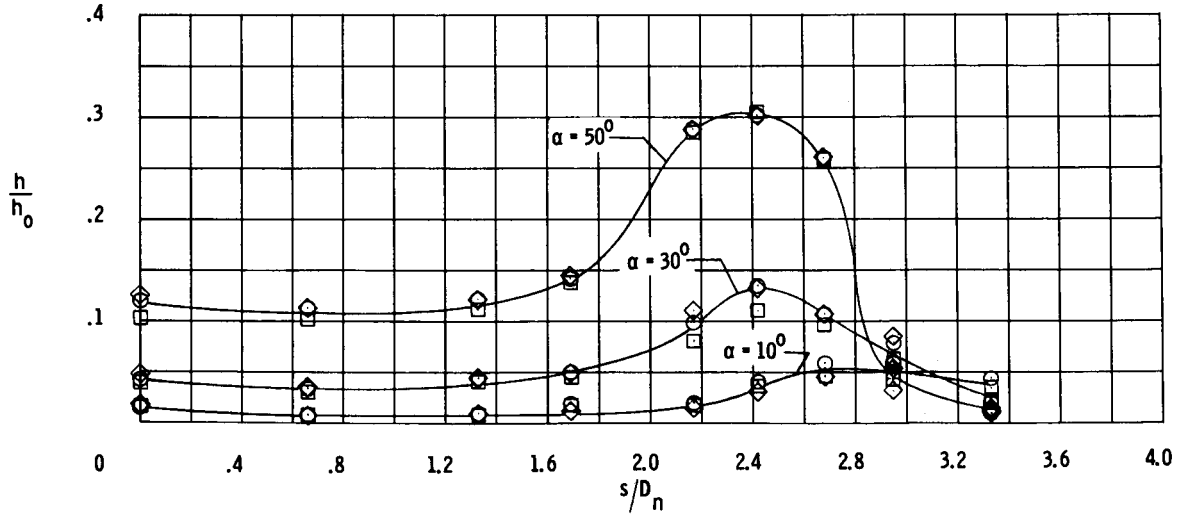

(b) x/c = 0.750.

Figure 12.- Summary of spanwise heat-transfer distribution for three angles of attack and elevon deflections.

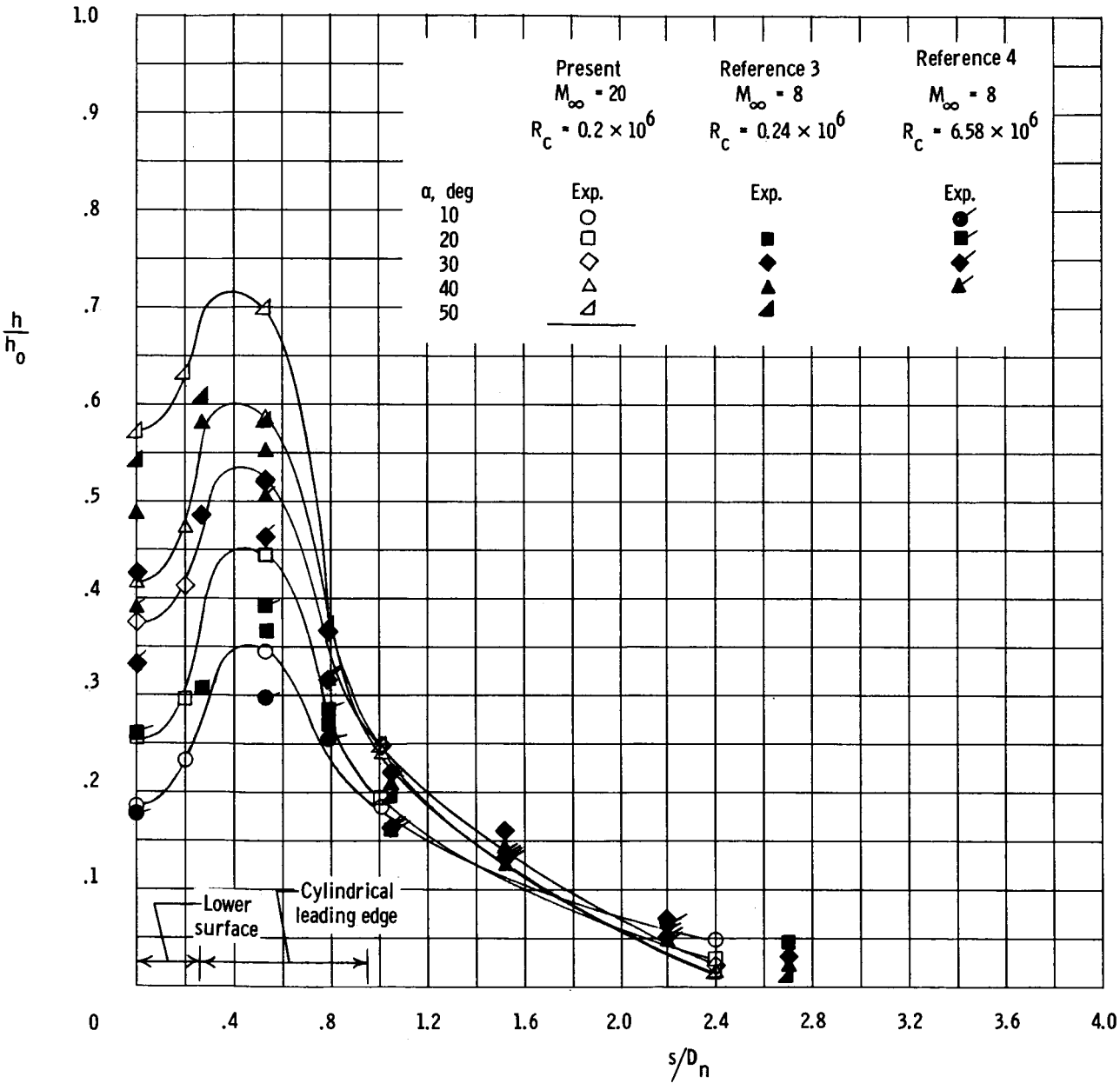

(a) x/c = 0.125.

Figure 13.- Comparison of present spanwise heat-transfer distribution with Mach 8 results for representative chordwise stations. $\delta_e = 0^0$.

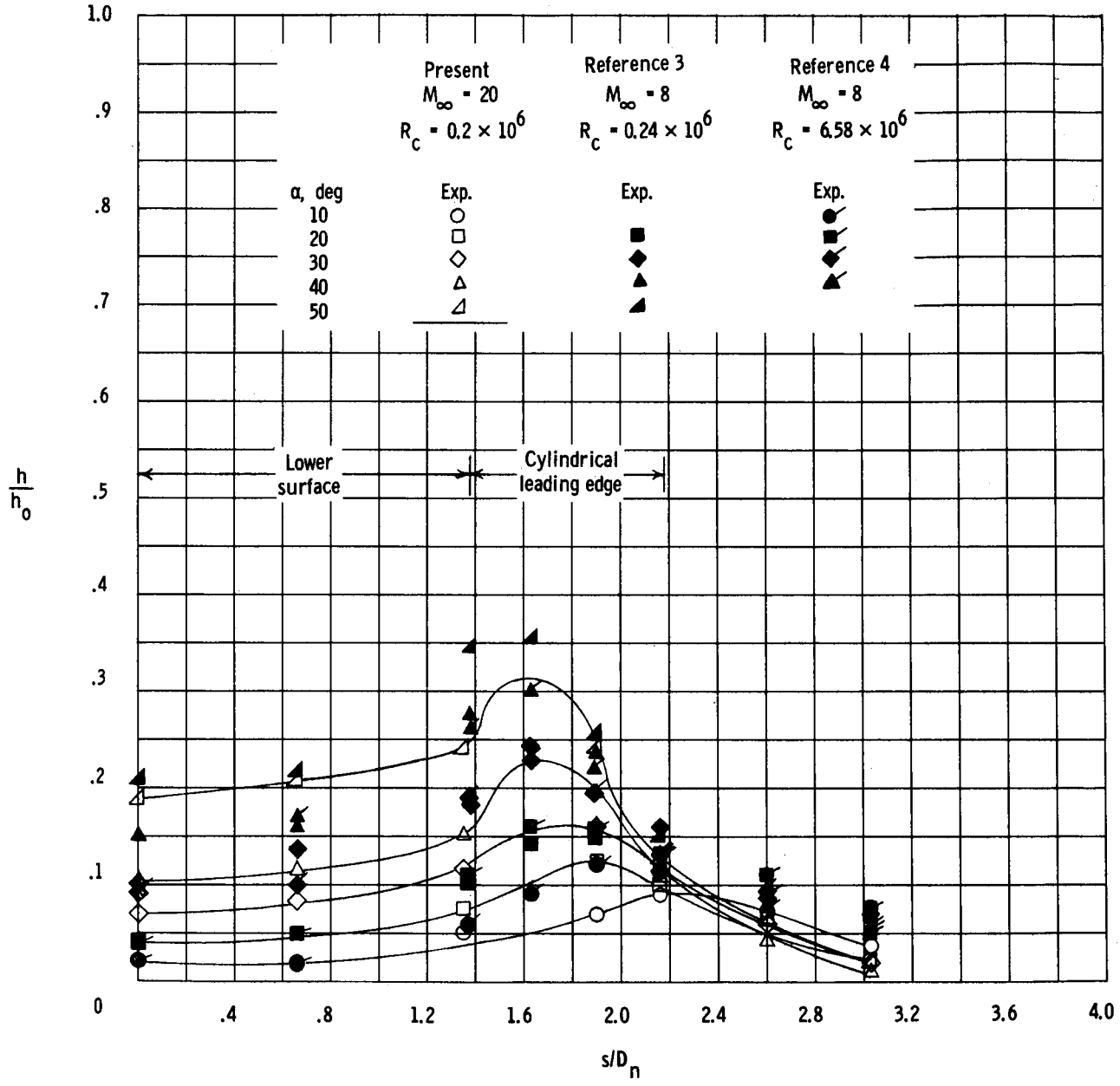

(b) x/c = 0.500.

Figure 13.- Concluded.

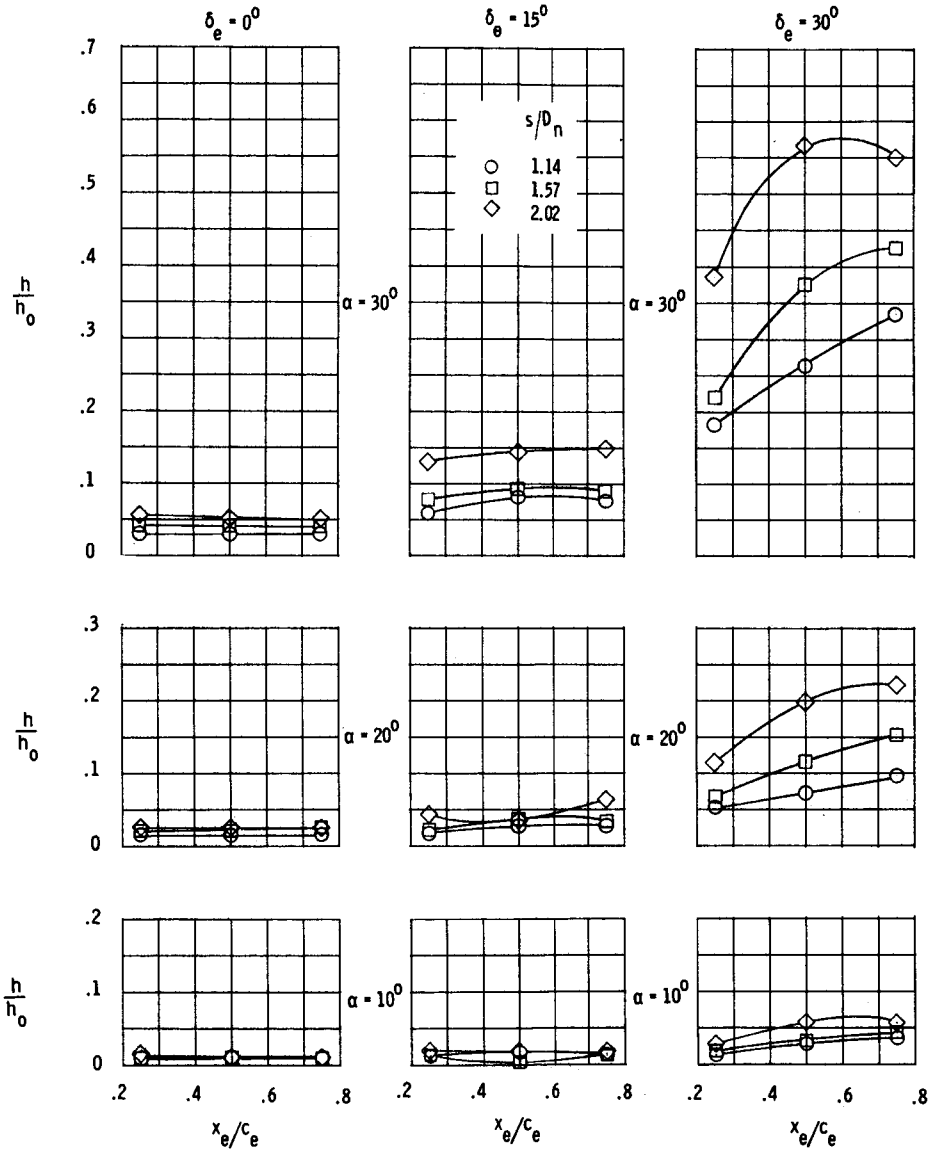

Figure 14.- Chordwise heat-transfer distribution on elevons.

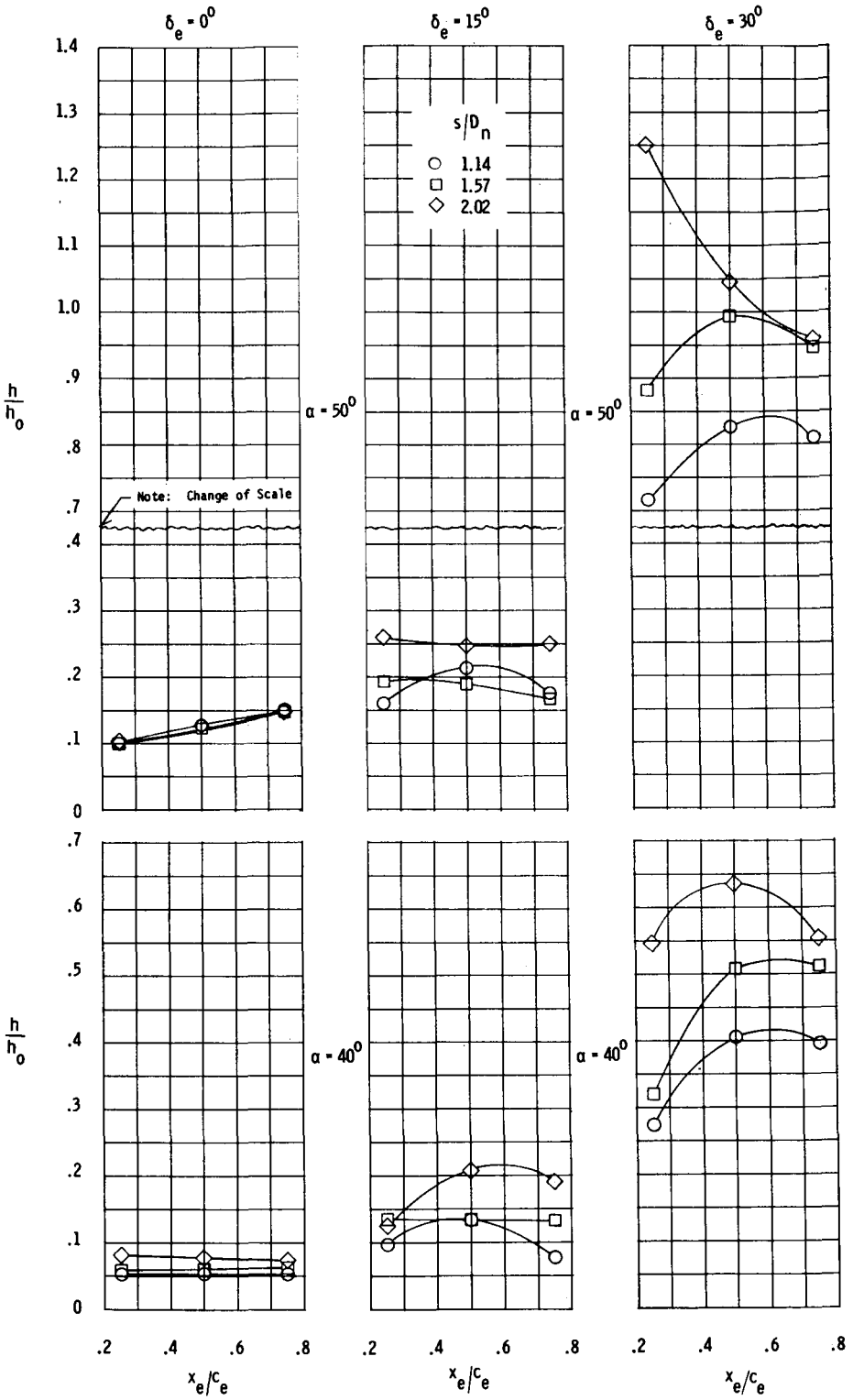

Figure 14.- Concluded.

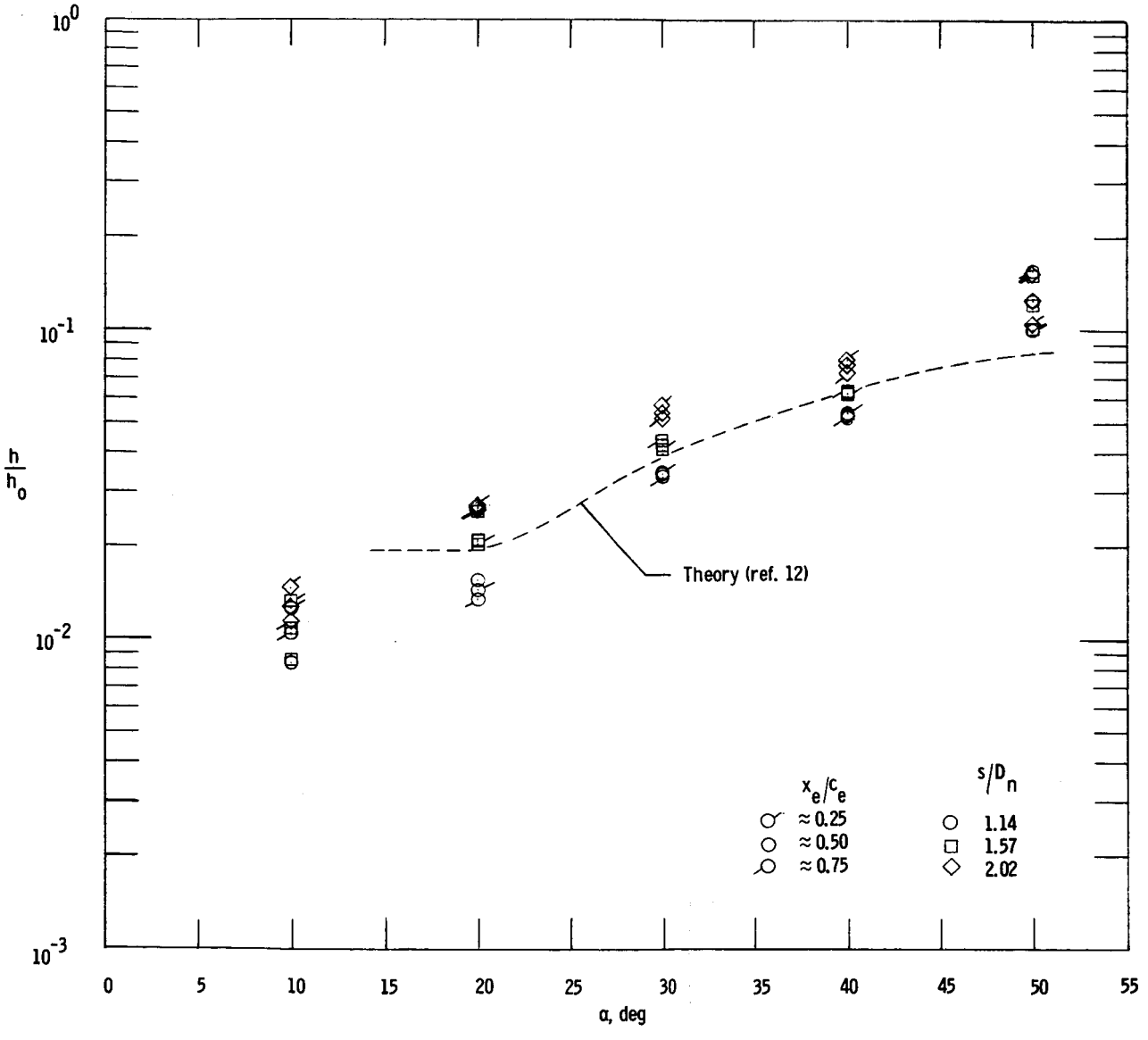

(a) $\delta_e = 0^o$.

Figure 15.- Summary of heat-transfer distribution on lower surface of elevons.

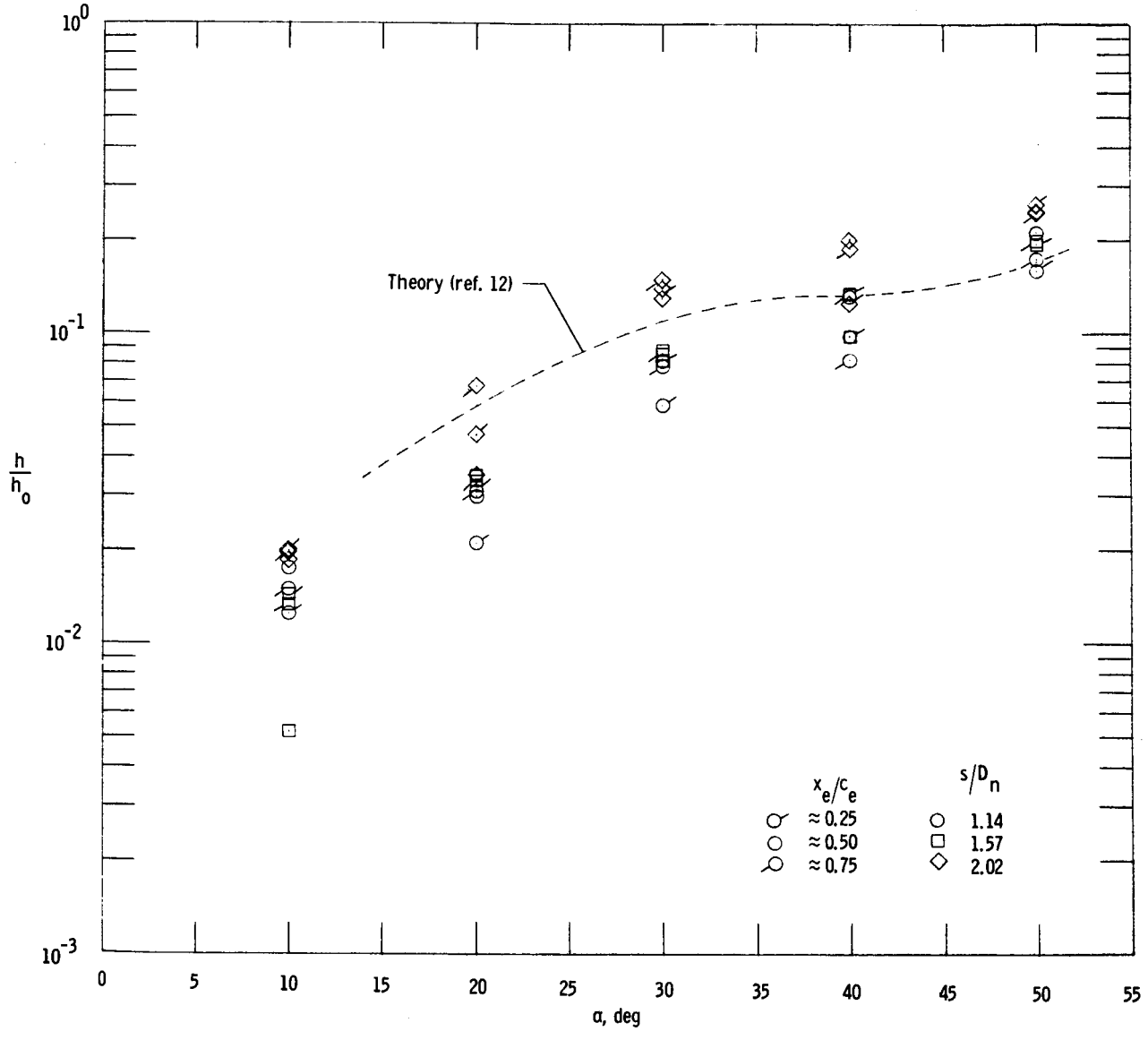

(b) $\delta_e = 15^0$.

Figure 15.- Continued.

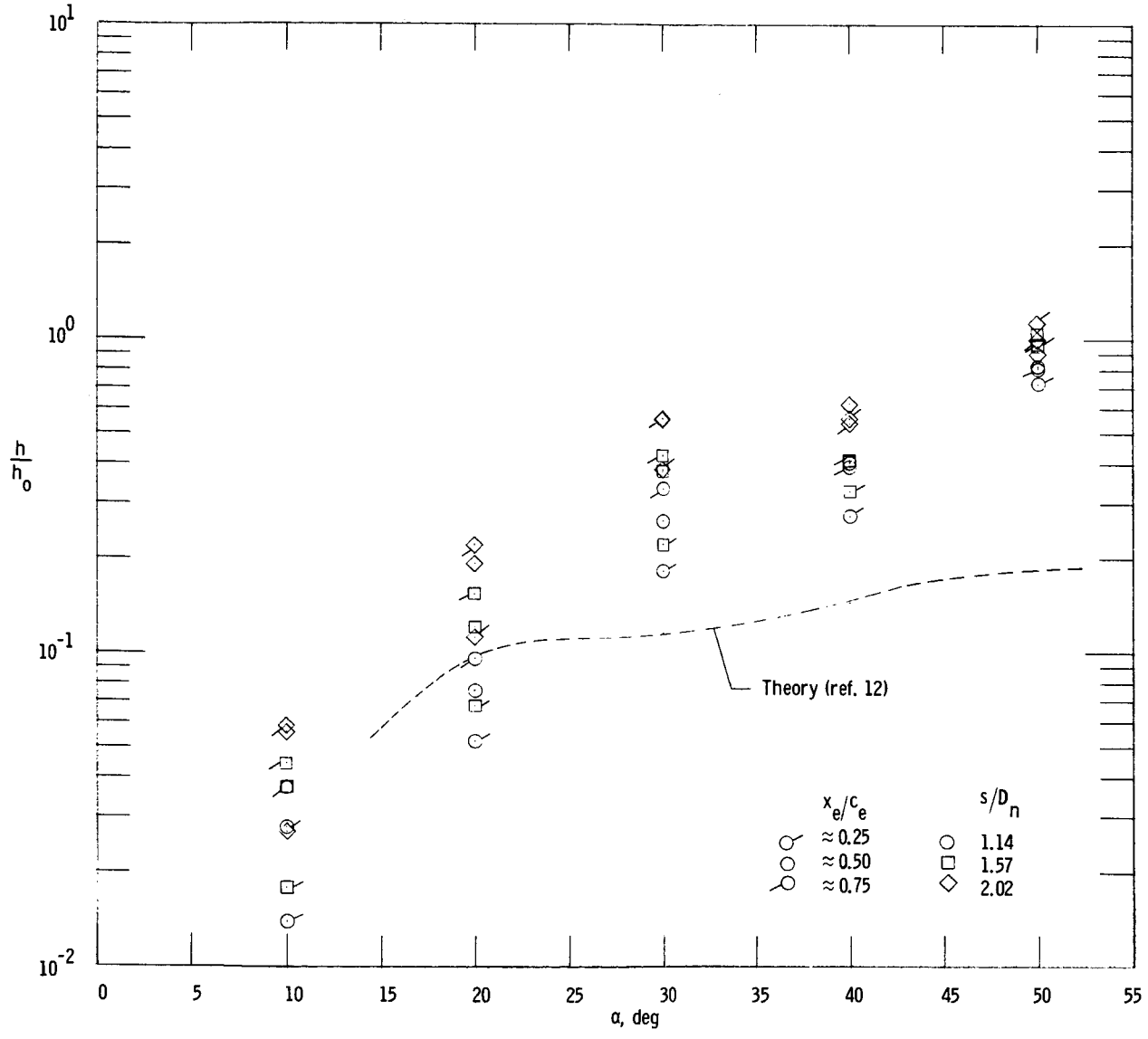

(c) $\delta_e = 30^0$.

Figure 15.- Concluded.

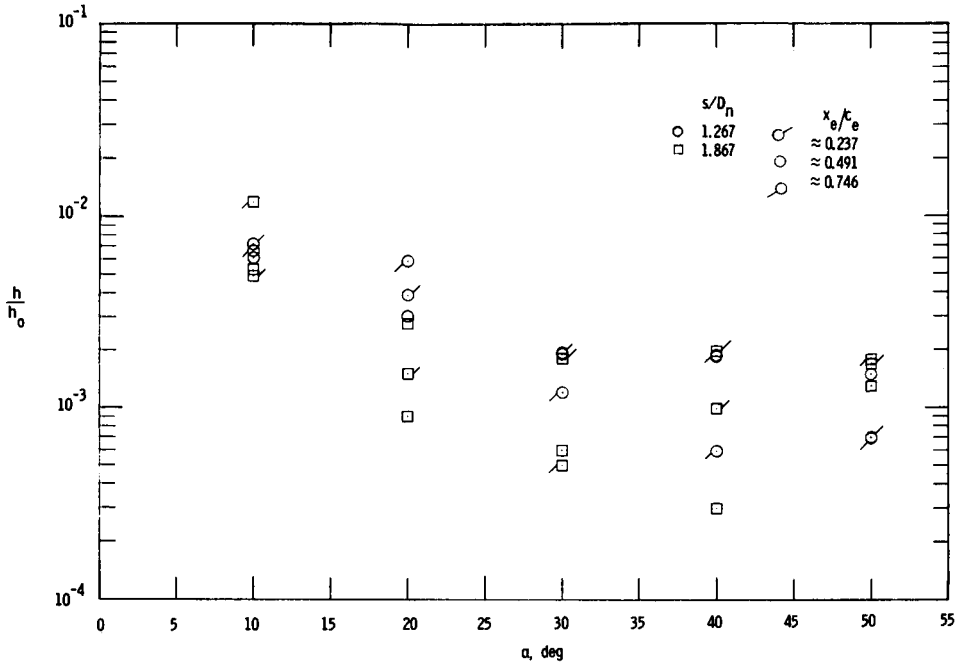

(a) $\delta_e = 0^o$.

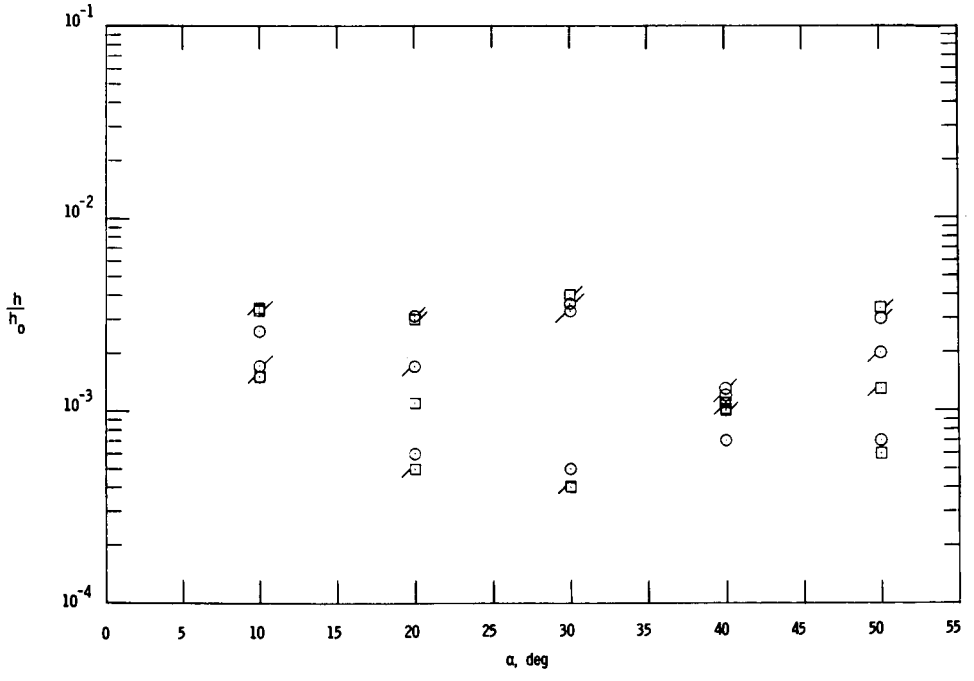

(b) $\delta_e = 30^o$.

Figure 16.- Summary of heat-transfer distribution on elevon upper surface.

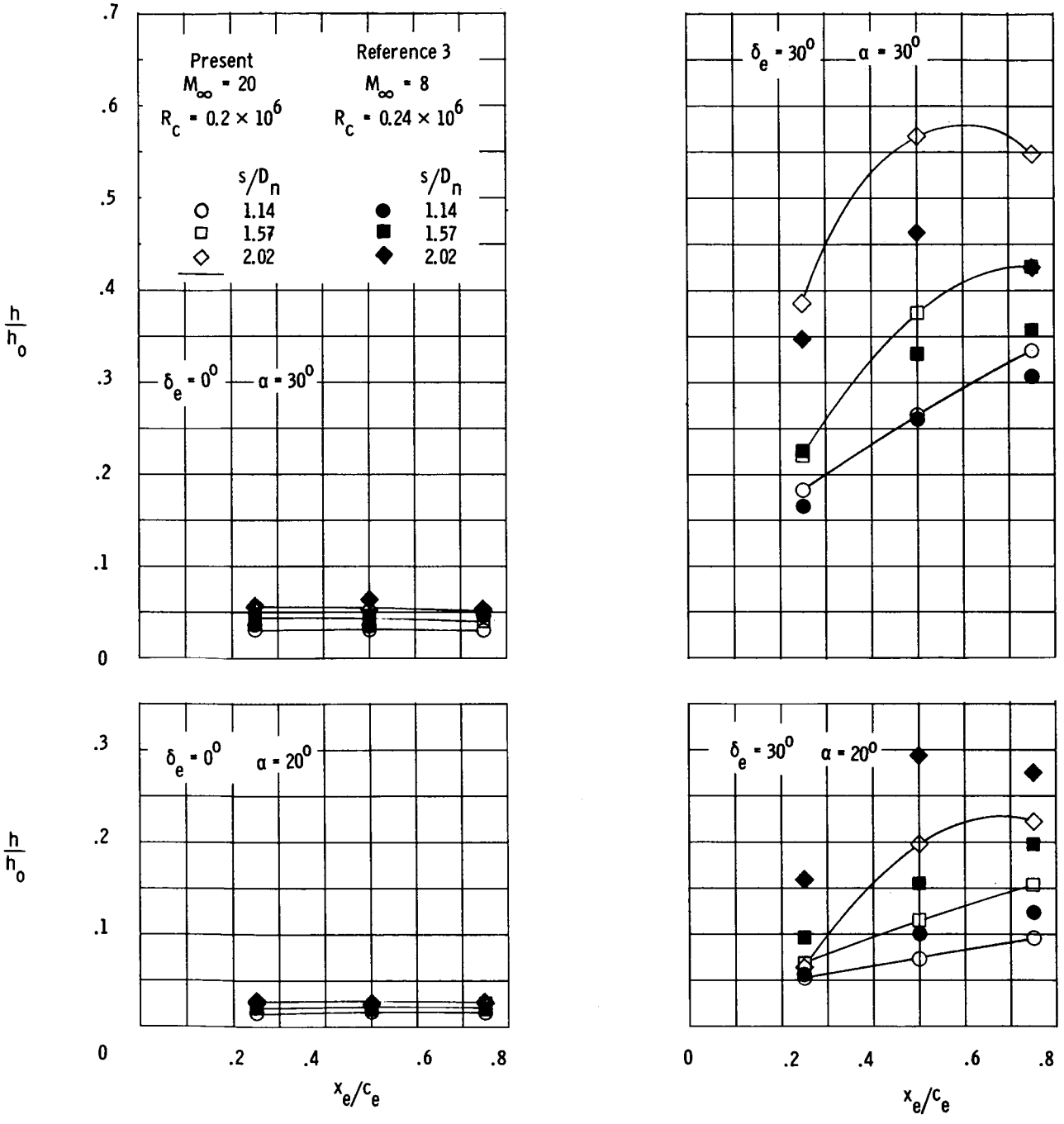

Figure 17.- Comparison of present chordwise heat-transfer distribution on elevons with Mach 8 results.

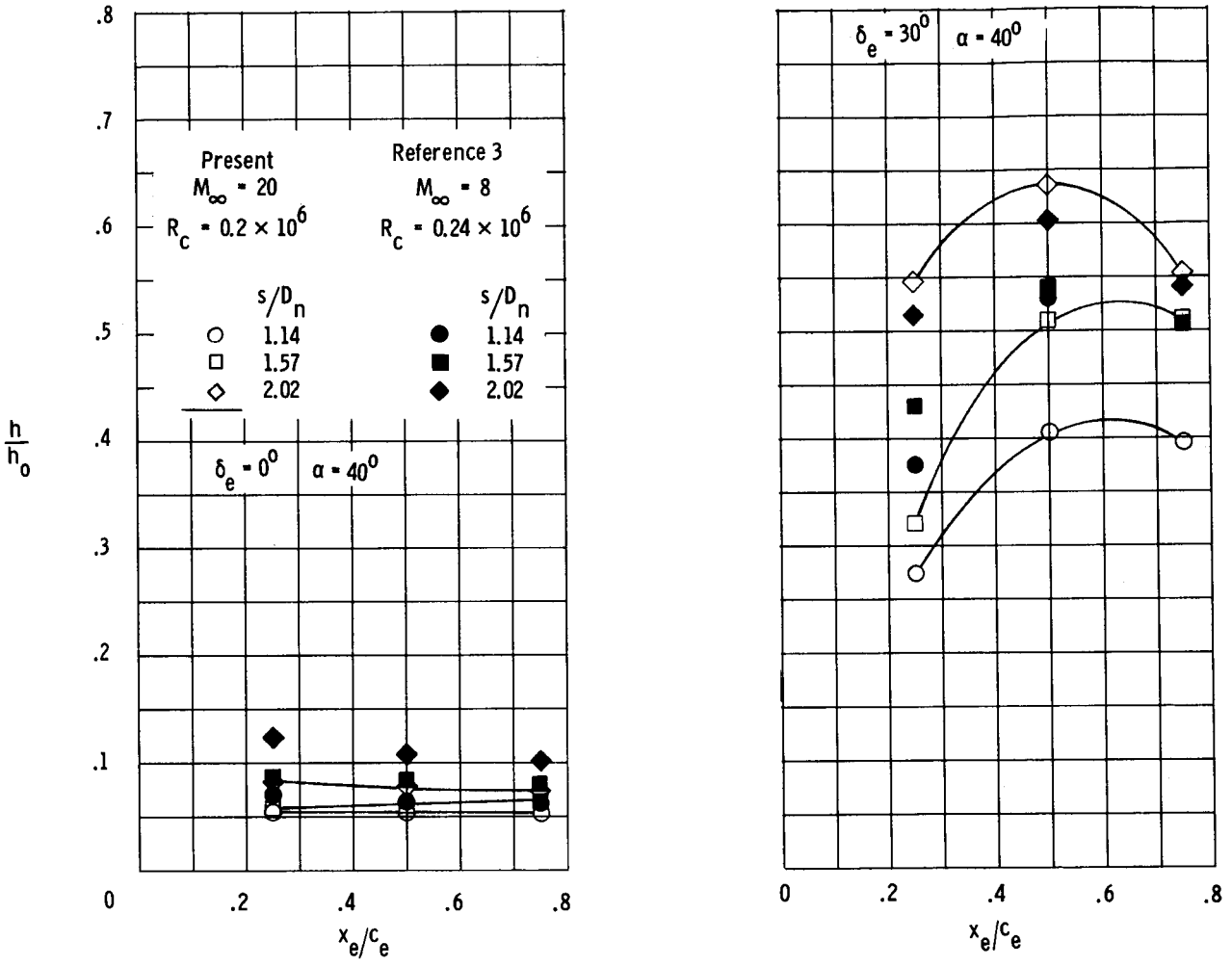

Figure 17.- Concluded.

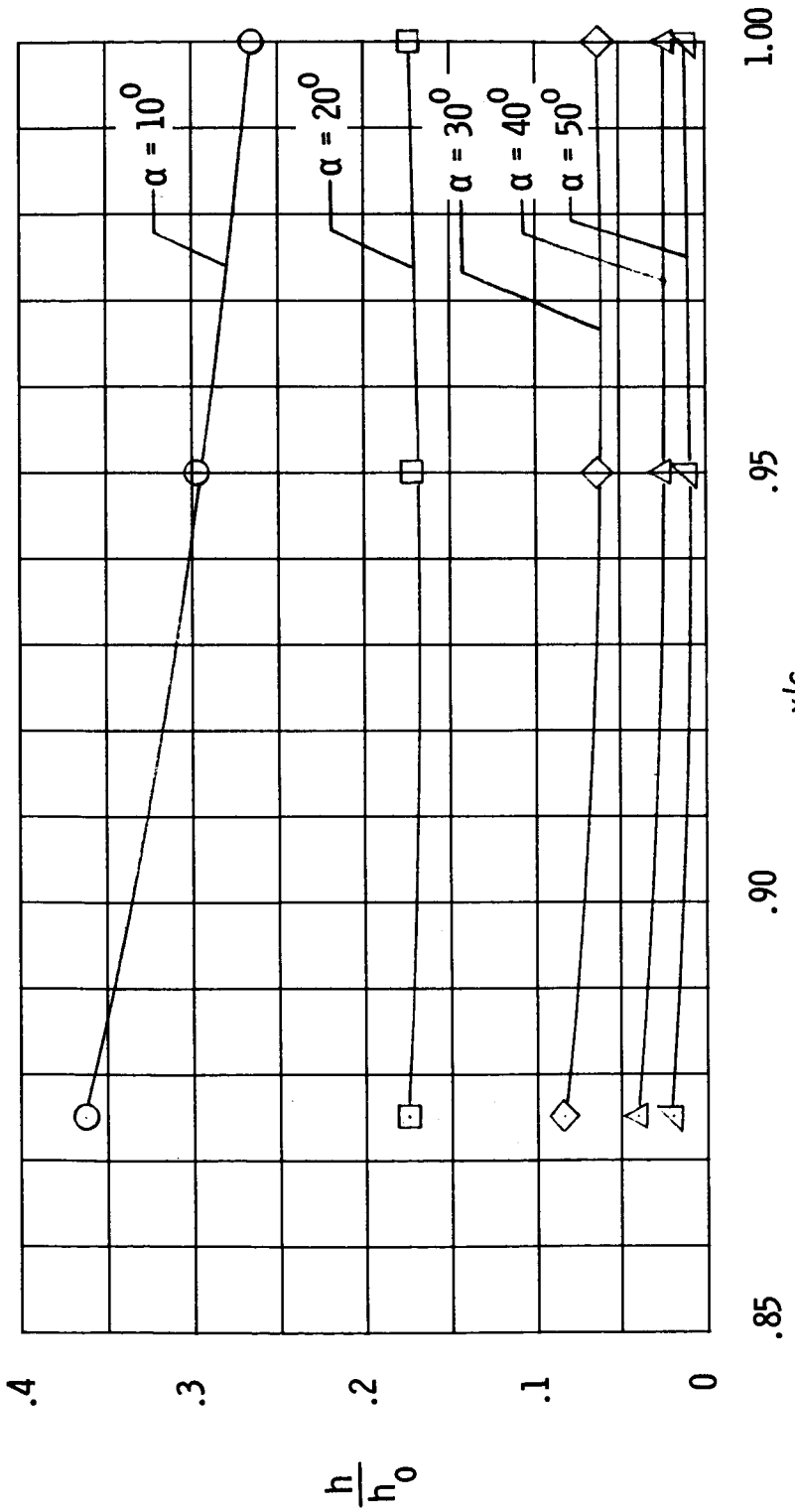

Figure 18.- Heat-transfer distribution on leading edge of tip fin for angles of attack. $\delta_e = 0^\circ$.

"The aeronautical and space activities of the United States shall be conducted so as to contribute . . . to the expansion of human knowledge of phenomena in the atmosphere and space. The Administration shall provide for the widest practicable and appropriate dissemination of information concerning its activities and the results thereof."

—NATIONAL AERONAUTICS AND SPACE ACT OF 1958

NASA SCIENTIFIC AND TECHNICAL PUBLICATIONS

TECHNICAL REPORTS: Scientific and technical information considered important, complete, and a lasting contribution to existing knowledge.

TECHNICAL NOTES: Information less broad in scope but nevertheless of importance as a contribution to existing knowledge.

TECHNICAL MEMORANDUMS: Information receiving limited distribution because of preliminary data, security classification, or other reasons.

CONTRACTOR REPORTS: Technical information generated in connection with a NASA contract or grant and released under NASA auspices.

TECHNICAL TRANSLATIONS: Information published in a foreign language considered to merit NASA distribution in English.

TECHNICAL REPRINTS: Information derived from NASA activities and initially published in the form of journal articles.

SPECIAL PUBLICATIONS: Information derived from or of value to NASA activities but not necessarily reporting the results of individual NASA-programmed scientific efforts. Publications include conference proceedings, monographs, data compilations, handbooks, sourcebooks, and special bibliographies.

Details on the availability of these publications may be obtained from:

SCIENTIFIC AND TECHNICAL INFORMATION DIVISION

NATIONAL AERONAUTICS AND SPACE ADMINISTRATION

Washington, D.C. 20546